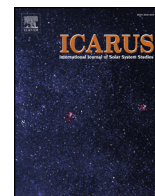




ELSEVIER

Contents lists available at ScienceDirect

Icarus

journal homepage: www.elsevier.com/locate/icarus

Transient eddies in the TES/MCS Ensemble Mars Atmosphere Reanalysis System (EMARS)

Steven J. Greybush^{a,b,*}, Hartzel E. Gillespie^a, R. John Wilson^{c,d}

^a Department of Meteorology and Atmospheric Science, The Pennsylvania State University, University Park, PA, USA

^b Department of Atmospheric and Oceanic Science, University of Maryland, College Park, MD, USA

^c NOAA/Geophysical Fluid Dynamics Laboratory, Princeton, NJ, USA

^d NASA Ames, Moffett Field, CA, USA

ARTICLE INFO

Keywords:

Atmospheres

Dynamics

Mars, atmosphere

Meteorology

ABSTRACT

Transient eddies are important features of Mars atmosphere weather, and are linked to the genesis of dust storms. Many previous studies of transient eddies, also known as traveling waves, generally used either spacecraft observations or model simulations alone. Reanalyses, which optimally combine observations with a forecast model, provide an unprecedented opportunity to examine these traveling weather systems: their temperature, wind, pressure signatures and structure; the evolution between various wave regimes; and their seasonality and interannual variability. Using the GFDL Mars Global Climate Model (MGCM) with the Local Ensemble Transform Kalman Filter (LETKF), we have created a six year reanalysis of both Thermal Emission Spectrometer (TES) and Mars Climate Sounder (MCS) temperature retrievals, which we name the Ensemble Mars Atmosphere Reanalysis System (EMARS). We demonstrate that the transient eddies in analyses with different assumptions in the model and assimilation system, including between EMARS and the Mars Analysis Correction Data Assimilation reanalysis (MACDA), are generally robust; EMARS and MACDA eddies are more similar to each other than their respective freely running control simulations. We also reveal lower atmosphere transient eddies derived from MCS data for the first time, and compare to those derived from TES data. MCS, as a limb sounder, demonstrates some challenges in constraining the shallow eddies in EMARS compared to reanalyses using TES nadir measurements. Ensemble reanalyses are valuable in that they provide an assessment of convergence upon a unique synoptic state. We examine the six year climatology and interannual variability of transient eddies, synoptic maps, and transitions between dominant wavenumber regimes. Finally, we compare reanalysis products to other products derived from observational data, including radio science and the Viking lander surface pressure records.

1. Introduction

Traveling weather systems on Mars, like those on Earth, are a key component of planetary meteorology. These weather systems are synonymously referred to as traveling waves or transient eddies. Found along mid-latitude meridional temperature gradients, eddies serve an essential role in transporting heat poleward. The extratropical weather patterns during autumn, winter, and spring seasons on Mars tend to feature eddies of several zonal wavenumbers, with a particular wavenumber dominating the eddy amplitude for a length of time; the transition between these wavenumber regimes provides a source of interannual variability to Martian weather. Finally, the wind field associated with these cyclones is linked to the genesis of dust storms, one of Mars's most visually evident atmospheric features. Transient eddies in the Martian atmosphere can be

quite vertically extended; however lower atmosphere transient eddies (e.g. below ~ 300 Pa) are the focus of this study, as they are responsible for contributing to the wind stress that mobilizes dust at the surface. Lower atmosphere waves appear to be dominated by baroclinic energy exchange, whereas the deeper (and longer) waves most prominent at higher altitudes (e.g. Barnes et al., 1993; Wilson et al., 2002) have a significant barotropic energy component (e.g. Greybush et al., 2013). Here, we will focus on the observed seasonality, wavenumber / wave period, and spatial structure of the eddies; a more complete and detailed description of the observed and modeled characteristics of Martian transient eddies can be found in Barnes et al. (2017).

A striking feature of the seasonality of Martian transient eddies is the “solstitial pause,” a decrease in the amplitude of transient eddies near the winter solstice relative to the maxima in fall and late winter/

* Corresponding author at: Department of Meteorology and Atmospheric Science, The Pennsylvania State University, University Park, PA, USA.

E-mail address: sjg213@psu.edu (S.J. Greybush).

<https://doi.org/10.1016/j.icarus.2018.07.001>

Received 26 October 2017; Received in revised form 18 May 2018; Accepted 5 July 2018

Available online 02 August 2018

0019-1035/ © 2018 Elsevier Inc. All rights reserved.

early spring seasons. Surface pressure and wind observations by the Viking landers suggested that eddy amplitudes were greatest in the late winter and early spring seasons (Barnes, 1980). The Thermal Emission Spectrometer (TES) (Smith et al., 2001) aboard Mars Global Surveyor (MGS) provided vertical profiles of temperature that were instrumental to understanding transient eddies; TES observed a reduction in eddy activity near the winter solstice (Wang et al., 2005). Modern Mars global circulation models (MGCMS) produce the solstitial pause as well (Basu et al., 2006; Kavulich et al., 2013;), but the details of wave amplitudes and seasonality show sensitivity to aerosol forcing which invites further exploration (Mulholland et al., 2016; Lee et al., 2018).

Observations have provided constraints on wave period and wavenumber of transient eddies. Martian eddies were noted to be very regular by Barnes (1980) in his examination of the Viking data, with the dominant transient wave periods in the energy spectra from Viking 2 were 6.7, 3.1, and 2.3 sols. The TES observations showed that there were dominant zonal wavenumbers of 1, 2, and 3 for lower atmosphere transient eddies in Mars years 24 through 26 (using the Clancy et al. (2000) Mars year convention) (Barnes, 2006; Hinson, 2006). These wavenumbers and periods in TES data likely correspond to the wave periods found in the Viking data, an idea which we explore here. Collins et al. (1996) found that there were rapid, abrupt transitions between dominant wave periods in the Viking data. Abrupt wave transitions were found in radio science (RS) observations, which have a near-surface vertical resolution finer than any other available observations (Hinson, 2006; Hinson et al., 2012). The model of Wang and Toigo (2016) produced rapid transitions between eddies with different wavenumbers. In particular, wavenumber 3 may be important in the study of dust storms. When wavenumber 3 eddies dominate, dust storms are a more frequent occurrence (Hinson et al. 2012). Furthermore, Wang et al. (2013) argued that regional dust storms enhanced transient eddies with zonal wavenumber 3. Wavenumber also affects spatial structure; transient eddies with larger wavenumbers are more confined to the surface in the models of Wilson et al. (2002), Kavulich et al. (2013), and Wang et al. (2013), just as in observations (Wilson et al. 2002; Banfield et al. 2004). A multiannual perspective on wave regime transitions from both TES and MCS eras would therefore complement and extend the existing literature.

Many observational sources, including TES and RS, as well as modern MGCMS provide insights on wave structure, including evidence that there is a westward tilt with height of Martian transient eddies (Banfield et al., 2004; Hinson and Wang, 2010) indicating that they are likely, at least in part, baroclinic Rossby waves. Models replicate the observed topographically induced increases in eddy amplitude over Arcadia, Acidalia, and Utopia, known as “storm zones” (Hollingsworth et al., 1996; Mooring and Wilson, 2015). Dust fronts are visible in Mars Orbital Camera (MOC) imagery (Cantor et al., 2001; 2007) as well as models (Hollingsworth and Kahre, 2010), and these fronts are likely associated with frontal boundaries between warm and cold air in passing transient eddies (Wang et al., 2003; 2005).

Up until recently, studies of transient eddies and their climatology and circulation fields have been limited by sparse observations or based on atmospheric model simulations. As noted above, these simulations capture many salient features of the available observations. However, further exploration of key issues in Martian meteorology, such as the interannual variability of eddy activity and the relationship between specific eddy events and dust lifting, require more extensive datasets. More recently, atmospheric reanalyses provide a comprehensive view of Mars atmosphere weather, combining both modeling and observational insights to provide our best estimate of the state of the atmosphere on a regular grid at specific time intervals. Reanalyses on Earth (e.g. Kalnay et al., 1996) are a highly utilized resource for understanding climatology as well as exploring case studies for specific weather events. It is anticipated that reanalyses should produce transient eddies that are more realistic (and more similar to observations) than atmospheric model simulations alone. An issue for Mars may be the much more limited set of observations, relative to those available for the terrestrial atmosphere. Because reanalyses include observational

information, they can be expected to possess transient eddies with propagation speeds, wavenumbers, and phases matching the observed waves, while also providing the full 3-D synoptic structure of specific eddies across several atmospheric fields (e.g. temperature, wind, and surface pressure) that are associated with specific observed dust lifting events. We review Mars atmosphere reanalyses and previous studies of their transient eddy characteristics in Section 2.

This study is the first to compare Martian transient eddy states in two different reanalyses to examine the robustness of these features, and characterize the confidence in the assessment of individual synoptic wave states. It is also the first to examine lower-atmosphere transient eddies in a Mars Climate Sounder reanalysis and compare them to waves from the Thermal Emission Spectrometer data for a more complete view (spanning six Mars years) of wave climatology, inter-annual variability, and regime transitions: a major aim of this study. The study also explores how differences in the observing systems may be manifested in the corresponding transient eddy characteristics in reanalyses. Finally, these datasets are compared to wave characteristics observed in situ by the Viking landers and by radio science observations. Section 2 describes the observational and reanalysis datasets, as well as the methodology for extracting transient eddy characteristics. Section 3 presents results on transient eddy structure, climatology, and sensitivity. Section 4 provides conclusions.

2. Data and methods

2.1. Spacecraft observations from TES and MCS

Two comprehensive datasets that provide multi-year and planetary-scale coverage of atmospheric conditions on Mars are obtained from the Thermal Emission Spectrometer (TES) and Mars Climate Sounder (MCS) instruments. TES flew aboard the Mars Global Surveyor (MGS) mission from 1999 to 2004. The TES nadir retrievals (Smith et al., 2001), available from the Planetary Data System (PDS), constitute the first global description of Martian weather, extending from Mars Year (MY) 24 to 27. Nadir temperature profiles (2x per sol) extend from the surface to ~40 km in the vertical on 21 vertical levels, with 2–5 effective vertical degrees of freedom in the vertical. Profiles therefore contain considerable vertical smoothing. Also included are column opacity (daytime only) for dust and water ice. PDS retrievals have unrealistic interannual variability at low levels, which is indirectly associated with changes in spectral resolution of TES (from MY 25 ~Ls = 100° to MY 26 ~Ls = 100°) (Wilson et al., 2014). TES retrievals at low altitudes over the winter poles also exhibit temperatures that are unrealistically below the supersaturation critical temperature with respect to CO₂. A comparison of the PDS TES retrievals with those derived using Optimal Spectral Sampling (OSS; Moncet et al., 2008; Eluszkiewicz et al., 2008) is found in Hoffman et al. (2012). Further discussion of instrumental issues can be found in Pankine (2015; 2016).

MCS (McCleese et al., 2007) has been flying aboard the Mars Reconnaissance Orbiter (MRO) since 2006. Unfortunately, there is no temporal overlap between the TES and MCS instrument record, as the TES instrument failed before the MCS mission began. As it points to the limb, MCS provides greater vertical resolution than TES, as well as retrieved profiles of temperature, dust, and water ice to more than 80 km in altitude (Kleinböhl et al., 2009). The new cross-track observational strategy (Kleinböhl et al., 2013) allows 6 local times to be observed, providing a better observational constraint on the diurnal cycle of temperature and aerosol. MCS retrievals are provided on 105 vertical pressure levels, whereas the vertical averaging functions indicate an effective vertical resolution of 5 km. The latest 2D retrievals (Kleinböhl et al., 2017) provide superior capabilities in regions of sharp temperature gradients, such as the polar vortex. Here, we assimilate “version 5” MCS retrievals (2D retrievals) and both along-track and cross-track observations when available, unless otherwise stated. Challenges with the MCS retrievals include limited coverage in cases of

high opacity (Shirley et al., 2015), missing observations for aphelion season tropical afternoons, and limited sensitivity (being limb observations, there is some interference with the lower boundary) to the lowest few km of the atmosphere.

2.2. EMARS

The Ensemble Mars Atmosphere Reanalysis System (EMARS) combines information from spacecraft observations with information from an atmospheric model to create a gridded dataset of important atmospheric variables under the paradigm of data assimilation. Data assimilation uses a Bayesian framework under which a prior (also known as a “background” or “first guess”, typically a short term model forecast) is combined with observations, weighted by their respective accuracies, to create a posterior (or “analysis”). A sequence of analyses spanning a long period of time (e.g. several years) constitutes a reanalysis. While several studies have applied data assimilation to Mars (e.g. Lewis and Read, 1995; Houben, 1999; Zhang et al., 2001; Lewis et al., 2007; Hoffman et al., 2010; Lee et al., 2011; Steele et al., 2014; Navarro et al., 2014; Navarro et al., 2017), the Mars Analysis Correction Data Assimilation (MACDA; Montabone et al., 2014) is the first comprehensive Mars reanalysis; EMARS is currently the only alternative, and the first ensemble Mars reanalysis. EMARS products have been used to study the thermal tides and water ice clouds (Zhao et al., 2015), Martian polar vortex (Vaughn et al., 2016), and now Mars atmosphere transient eddies. The model and data assimilation system used for EMARS are described in detail in Greybush et al. (2012) and Zhao et al. (2015); highlights and upgrades, in particular for the assimilation of MCS observations, as well as comparisons with MACDA, are described here. EMARS grid spacing is 6° longitude by 5° latitude. The vertical coordinate is a hybrid sigma-pressure coordinate, with terrain-following sigma levels near the surface transitioning to pressure levels above 2 Pa. The model contains 28 vertical levels, with 13 of these levels being in the lowest scale height of the atmosphere. The vertical grid spacing increases substantially with height.

EMARS uses the Local Ensemble Transform Kalman Filter (LETKF; Hunt et al., 2007), a type of ensemble Kalman filter (EnKF; Evensen, 1994) where the flow-dependent uncertainty of the background is sampled in a Monte Carlo manner from an ensemble of atmospheric states; this offers a significant advantage compared to other assimilation techniques (Kalnay et al., 2007). The data assimilation system updates the temperature field by noting the difference between observations and model (observation increment), calculating an update based on the relative uncertainties of the two datasets (an analysis update), and spreading the information spatially in a local region based on flow-dependent error covariances. These inter-variable relationships are a strength of ensemble data assimilation methods, and allow an update of the wind and pressure field in a way that exhibits a reasonable geophysical balance (e.g. Greybush et al., 2011). The ensemble spread (standard deviation) provides information on the uncertainty associated with the analyses; errors arise from small initial condition differences that are amplified by atmospheric instabilities (e.g. Greybush et al., 2013), as well as model forcing errors such as those found in the representation of the vertical distribution of aerosols. Ensemble spread is tuned using the adaptive inflation technique (Miyoshi, 2011) to enforce the spread/skill relationship outlined in Desroziers et al. (2005) that ensemble variance plus the observation error variance matches the error variance of the short term forecasts compared to observations. A horizontal R-localization (Greybush et al., 2011) of 600 km is employed to limit the impact of spurious correlations among the 16 ensemble members on the shape of the analysis increments. Assimilation is conducted hourly to avoid artificial excitation of resonantly-enhanced tidal modes (Zhao et al., 2015).

A forward operator is used to convert variables in model space to variables in observation space, enabling a fair comparison between the two. A simplistic forward operator takes temperatures on the model

vertical coordinates, and interpolates them to TES and MCS levels. However, retrievals effectively represent a vertically integrated measure of temperature, especially for the PDS TES retrievals which have significant vertical smoothing and about 2–5 degrees of freedom in the vertical. Therefore, both observations and model temperature profiles are averaged in the vertical according to weighting functions appropriate to the particular instrument whose observations are being assimilated before being compared to compute observation increments. For TES, the 5 averaged levels of Montabone et al. (2014) are used; for MCS, with its greater vertical resolution, 21 averaged levels are used. This is a step toward properly using retrieval averaging kernels in assimilation, as outlined in Hoffman (2010). The sensitivity to forward operator is explored in Section 3.

EMARS employs the GFDL Mars Global Climate Model (MGCM; Wilson and Hamilton, 1996; Kavulich et al., 2013; Kleinböhl et al., 2013) in its finite volume, latitude/longitude dynamical core configuration. Column dust opacities are constrained by the dust scenarios compiled for the Mars Climate Database Version 5 (Montabone et al., 2015), which is a comprehensive gridded and interpolated product combining many dust opacity observations, mainly TES column opacities during the MGS mission and extrapolated MCS dust opacities during the MRO mission. The opacities are scaled by 70% to 130% among the ensemble members to provide ensemble spread by representing uncertainties in aerosol heating. The vertical representation of dust is controlled by three radiatively active tracers, with particle radii of 0.3, 1.2, and 2.5 μm . As in Kahre et al. (2009), dust is added or subtracted from the lowest model levels (the boundary layer) to match the observed column opacities. The improved representation of dust using assimilation of MCS aerosol vertical profiles or thermal signatures (e.g. Navarro et al., 2014) is not applied in this version of EMARS. Radiatively active water ice clouds are employed, with varying opacities among ensemble members. A sub-grid-scale topographic gravity wave drag parameterization is used.

The MGCM has an active, multi-phase CO₂ cycle. When temperatures are projected to be below the (pressure-dependent) CO₂ critical temperature in the atmosphere, the gaseous CO₂ mass needed to generate the appropriate latent heating is removed from the atmosphere and placed on the surface as CO₂ snow. There are no explicit CO₂ cloud microphysics. The LETKF analysis increments (which also update surface pressure) are adjusted to conserve global atmospheric mass. However, TES observations fall below the CO₂ critical temperature by several degrees (Colaprete et al., 2008), leading to an excess of deposition onto the CO₂ cap. To remedy this, observations below the critical temperature are modified to be at the critical temperature, allowing for a more realistic CO₂ seasonal cap cycle, as indicated by comparisons with the seasonal variation of surface pressure at the Viking landers. The sensitivity to this quality control choice is explored in Section 3.

2.3. MACDA

The MACDA version 1.0 reanalysis is the first for Mars (Montabone et al., 2006; Lewis et al., 2007; Montabone et al., 2014), spanning a period from northern summer in MY 24 to northern spring in MY 27. MACDA uses the UK-LMD GCM (Forget et al., 1999) with a spectral dynamical core and the analysis correction scheme (Lorenz et al., 1991), which has similarities to a nudging scheme. MACDA's horizontal resolution is 5°, with 25 vertical sigma levels (both of which are roughly similar to EMARS). Dust optical depth is derived from TES observations (and therefore is similar, but not exactly the same as, the dust scenario used for EMARS). The vertical distribution uses the analytically specified Conrath (1975) profile (rather than evolving dynamically as in EMARS), with seasonal and latitude variations as specified in Montmessin et al. (2004). CO₂ is removed from the atmosphere when the temperature falls below the critical threshold, and supersaturated TES profiles are not assimilated (for the reasons elaborated upon in the description of EMARS). Unlike EMARS, radiatively active water ice clouds are not included in MACDA 1.0.

A few studies have looked at transient eddies in MACDA (Kavulich et al., 2013; Mooring and Wilson, 2015; Lewis et al., 2016; Battalio et al., 2016; Battalio et al., 2018). The GFDL MGCM does not produce as much interannual variability as MACDA (Kavulich et al., 2013). Transient eddies in MACDA possess a westward tilt with height, and wavenumbers 2 and 3 dominate at low altitudes (Battalio et al., 2016). A solstitial pause in transient eddy activity is also evident in the MACDA data (Mooring and Wilson, 2015; Lewis et al., 2016; Battalio et al., 2016).

2.4. Transient eddy analysis

The Mars atmosphere contains variability on many time scales, including strong seasonal and diurnal changes. Therefore, in order to focus on transient eddies, a filter must first be applied to disentangle the impact of these other oscillations. Typically, a bandpass filter like the one implemented in Lewis et al. (2016) is used to eliminate thermal tides and quasi-stationary waves. We describe the Lewis et al. (2016) filter, which we use in this work, in the following. Elliptic filters are applied to the time series of model data to compute the eddy amplitude by removing waves with low and high frequency. The input time series is subtracted by the output of a low-pass 4th order elliptic filter applied to the input time series, with cutoff period 15 sols, ripple 0.001 dB allowed in the passband, and at least 50 dB attenuation in the stopband. This subtraction effectively removes climatological variability from the input data. This difference is then taken as input to a low-pass 6th order elliptic filter with cutoff period 1.3 sols, 0.1 dB ripple allowed in the passband, and at least 60 dB attenuation in the stopband. This low-pass filter removes the diurnal tide and its harmonics from the data. What remains after the latter filter is applied is eddy amplitude. Collectively, these elliptic filters constitute a band-pass filter, and are guaranteed to remove no more than 2.4% of the eddy amplitude of waves with periods between 1.3 and 15 sols.

Eddy variance (of fields such as temperature) is calculated as functions of longitude, latitude, height and time. Variances due to zonal wave 1–3 components of fields (as in Basu et al., 2006; Kavulich et al., 2013; Lewis et al., 2016) are also computed. To extract waves with specific wavenumbers, eddy vectors composed of temperatures across all longitudes of a latitude circle are multiplied by discretized sine and cosine waves with the desired zonal wavenumber (1, 2, and 3). The wave amplitude for the given wavenumber is the square root of the sum of squares of the two products (with the sine and cosine waves). Values are reported after using a 10-sol moving average. Vertically, reanalyses are kept on native terrain-following model levels to avoid artifacts from interpolation, as interpolation to pressure surfaces would lose much of the low-level information due to highly variable topographic height; in practice, this is approximately a fairly uniform height above the surface.

Anomaly correlations between EMARS and other runs were computed by calculating eddy temperatures at EMARS model level 23 (approximately $\sigma = 0.9$, hence nominally about 1.1 km above ground). MACDA outputs were interpolated to the horizontal resolution of EMARS before filtering. The maximum eddy temperature between 49°N and 75°N at each longitude and time available from the filtered data was determined (to account for the latitude changes in eddy maximum with season), producing a Hovmöller diagram. The covariance of the maximum eddy temperatures in EMARS and a comparison run was computed. The anomaly correlation is given by the quotient of the covariance and the standard deviations of the maximum eddy temperatures in EMARS and in the other run.

2.5. Viking lander observations

Viking surface pressure observations were prepared to enable climatological comparisons with EMARS. To compute the eddy amplitude in the Viking pressure data over a long period, the data was binned at intervals of 0.25 sols. Gaps of 1 sol or less in the binned data were filled by linear interpolation. Eddy pressures were computed using the elliptic filter mentioned in the previous section. The total pressure eddy amplitude plots

were made by smoothing these eddy pressures using a 10-sol centered moving average. EMARS surface pressures at the grid cell closest to Viking landers 1 and 2 were filtered using the aforementioned band pass filter, and the resulting eddy pressures were smoothed using a 10-sol moving average.

3. Results and discussion

3.1. Transient eddy structure

An exploration of Mars atmosphere transient eddies in reanalyses begins with visualizing their structure. Fig. 1 shows synoptic (at the same time) maps of transient eddies: temperature, wind, and pressure eddy fields. These maps are not possible with observations (due to data sparsity) and model simulations (due to lack of connection with the conditions at a specific time in Mars history) alone. As EMARS assimilates temperature observations, the temperature field is expected to be the variable best constrained by observational data.

A representative snapshot of the TES-era transient eddy field is shown in Fig. 1a. This is a snapshot in an time interval when zonal wave

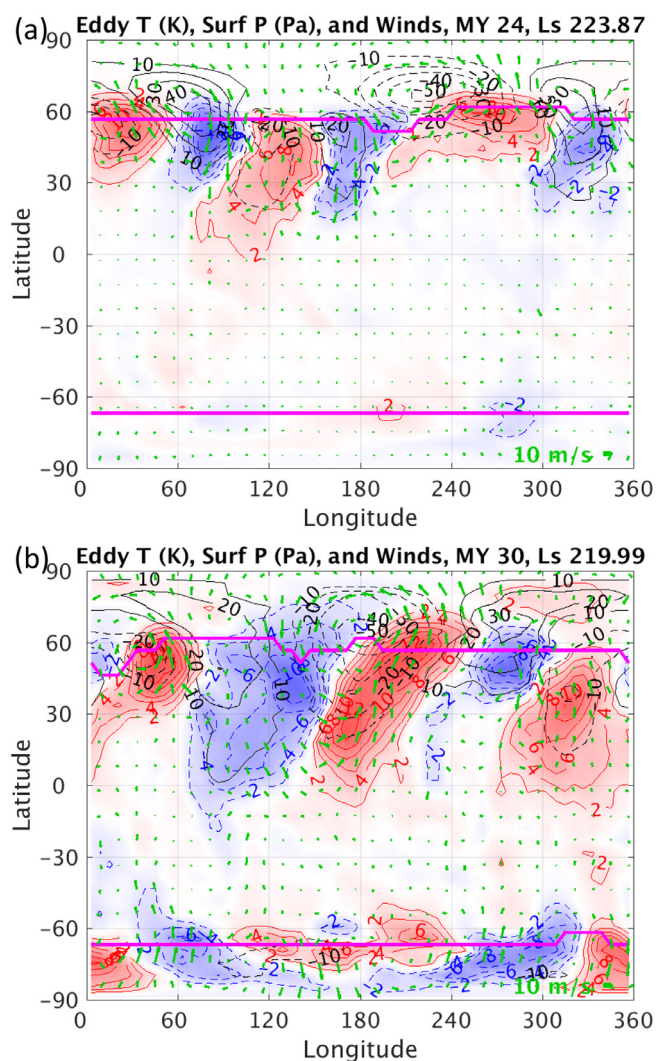


Fig. 1. Synoptic maps depicting the eddy field for EMARS at the model sigma level ~ 1 km above the surface during (a) MY 24 Ls 224, which is during the TES era, and (b) MY 30 Ls 220, which is during the MCS era. Eddy temperatures (K; red / blue shading and contours for warm / cold anomalies), eddy pressures (Pa; solid black contours for positive values, dashed black contours for negative values), and eddy wind field (green arrows pointing in the direction the wind is blowing towards). (For interpretation of the references to color in this figure legend, the reader is referred to the web version of this article.)

3 eddies were particularly prominent and lead to the initiation of the MY24 A season regional dust storm (Cantor et al., 2001; Wang et al., 2003). In this mid northern autumn (Ls 223.87) synoptic map, a zonal wave-3 pattern (easily seen in the eddy temperature field) is present in the northern hemisphere, with amplitudes of around 10 K. Note that the strongest temperature anomalies are located just south of 60 N, which is the latitude of the seasonal CO₂ ice cap edge at this time; the cap edge provides a natural near-surface temperature gradient. Anomalous high pressures (with amplitude around 40 Pa) are found near and just west of colder temperatures, with low pressure regions near and just west of warmer temperatures; these patterns are consistent with a hydrostatic atmosphere with waves that slope westward and poleward with height. The eddy wind field (with speeds ~10–20 m/s) approximates the isobars (quasi-geostrophically, when allowing for viscid,

isallobaric flow), with anticyclonic winds encircling high pressure areas and cyclonic flow around lows. This wind pattern advects lower temperatures equatorwards, and higher temperatures polewards.

For comparison, an MCS-era transient eddy is shown in Fig. 1b. As with the TES wave, a wave 3 structure spans the northern hemisphere, with a slightly greater latitudinal extent for the eddies. There is also transient eddy activity present in the southern hemisphere poleward of 60 S; we comment on this difference in Section 3.2. The selection of representative maps is based on viewing of animations, which indicate the eastward propagation of coherent features. The convergence of the reanalysis on a synoptic state will be discussed further later in the paper.

Figs. 2 and 3 show the vertical extent of the transient eddies via latitudinal and longitudinal cross sections. Note (in Fig. 2b, 2e) that there are separate waves in the lower atmosphere (e.g. below 300 mb)

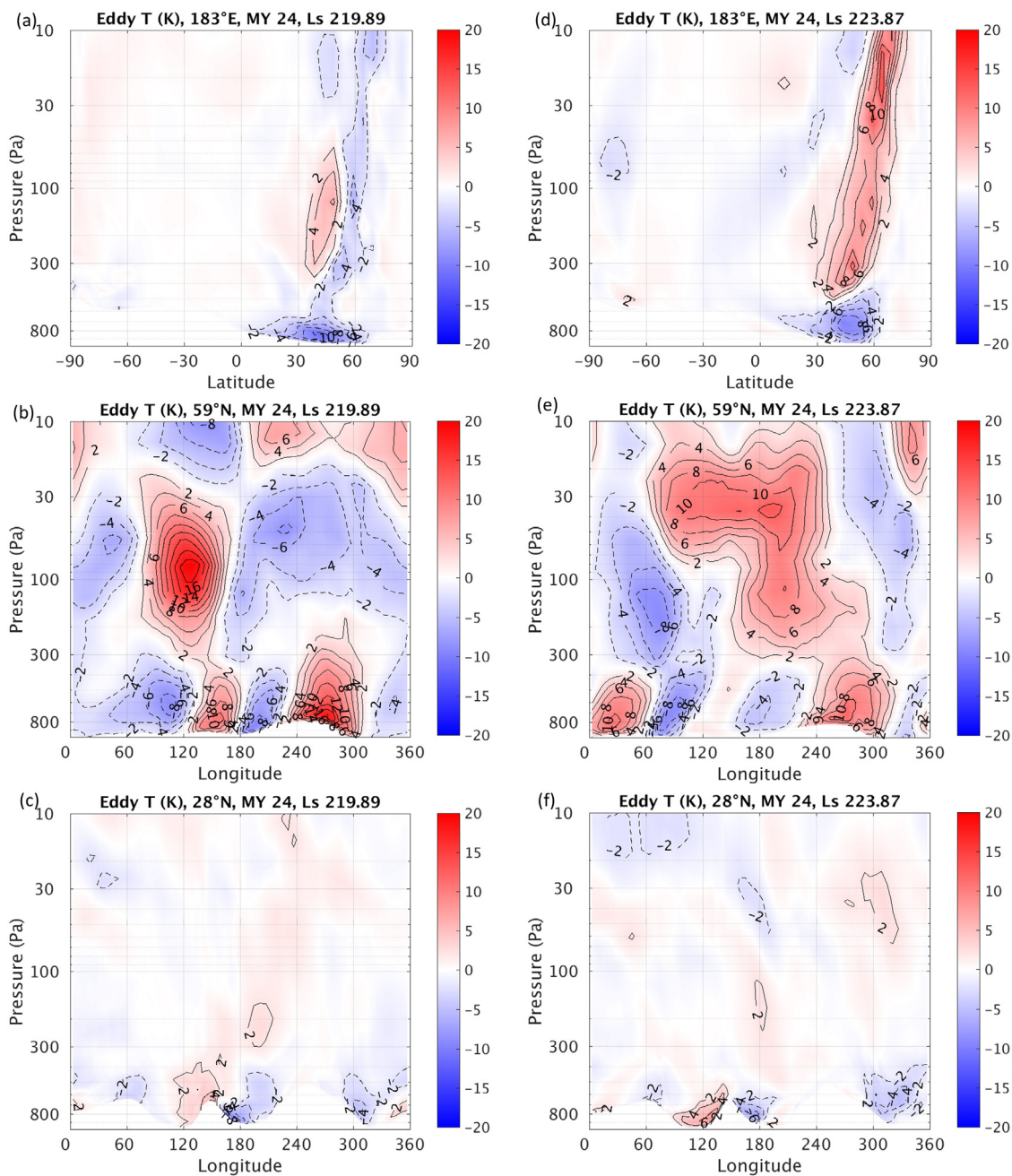


Fig. 2. Vertical cross sections of the eddy field for EMARS at MY 24 Ls 220 (a, b, c) and MY 24 Ls 224 (d, e, f), which correspond to the same time as Fig. 1a as well as 6.25 sols prior. (a, d) Vertical temperature structure (K; contours and shading) in a latitude-height cross section at longitude 183°E. Vertical structure in a longitude-height cross section at latitude (b, e) 59°N and (c, f) 28°N.

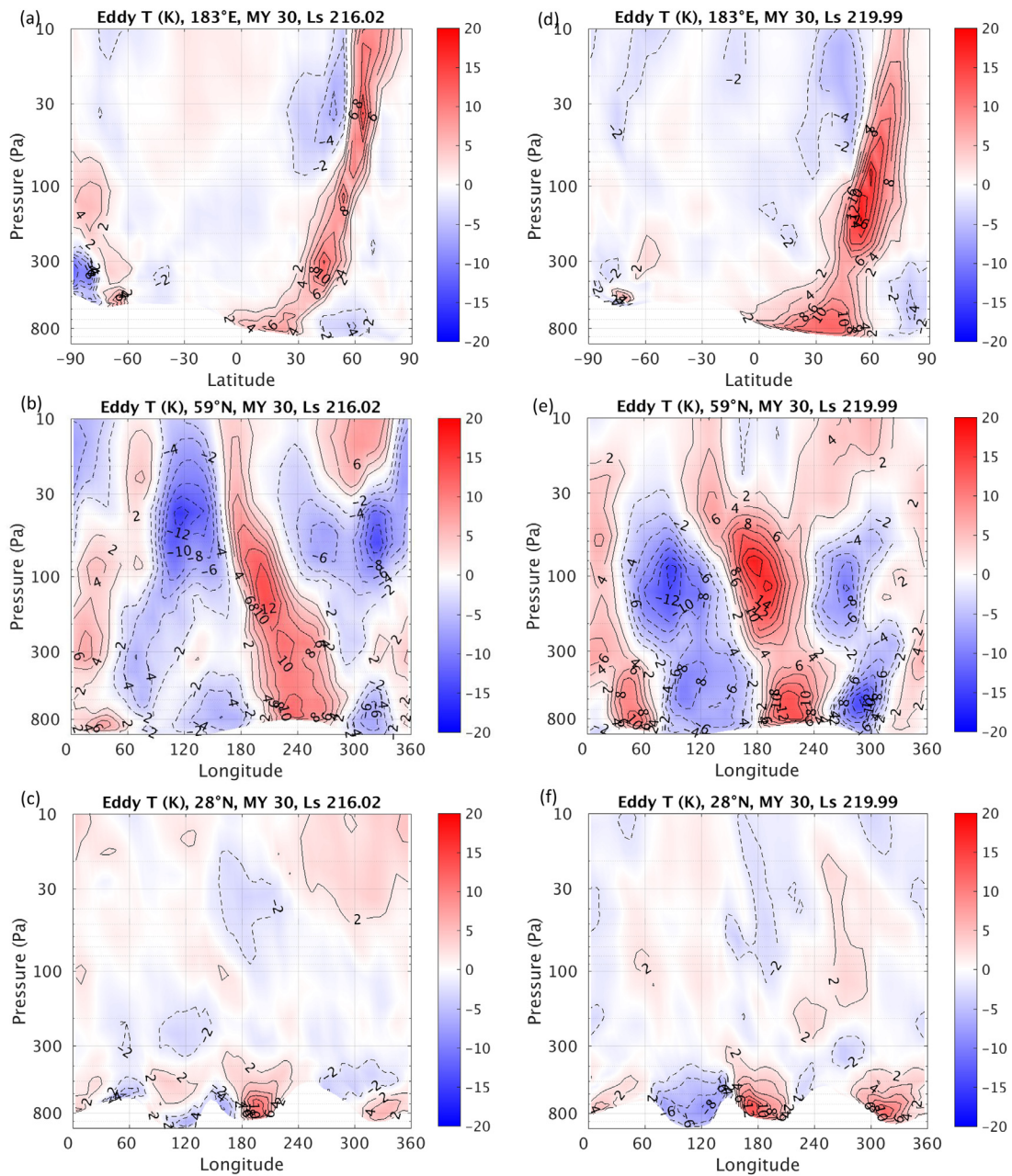


Fig. 3. Vertical cross sections of the eddy field for EMARS at MY 30 Ls 216 (a, b, c) and MY 30 Ls 220 (d, e, f), which correspond to the same time as Fig. 1b as well as 6.25 sols prior. (a, d) Vertical temperature structure (K; contours and shading) in a latitude-height cross section at longitude 183°E. Vertical structure in a longitude-height cross section at latitude (b, e) 59°N and (c, f) 28°N.

and the upper atmosphere (e.g. Greybush et al., 2013; Waugh et al., 2016). Zonal wave 1 is typically quite deep and is present in both the lower and upper atmosphere (Wilson et al., 2002; Lewis et al., 2016), whereas wave 2 is moderately deep (e.g. Fig. 3e) and wave 3 is largely confined to the lower atmosphere (e.g. Fig. 2e). The waves tilt poleward with height, following the structure of the polar vortex (Figs. 2a and 3a). The lower atmosphere waves can be in phase (e.g. Fig. 3d) or out of phase (e.g. Fig. 2d) with their upper altitude counterparts. Showing two separate cross sections 6.25 sols apart (left vs. right panels in Figs. 2 and 3) reveals that while the lower atmosphere waves have similar phasing, the upper atmosphere phases have changed. We are interested in the waves that lift dust from the surface, and hence focus on the lower atmosphere ones for this paper; using model level 23 (quasi-sigma

surface ~ 1 km above ground) for synoptic maps is therefore an appropriate choice. We also note the shallow extent of the lower atmosphere waves as they follow the lowland channels southward (Figs. 2c,f; 3c,f), which provides a challenge to constraining them observationally.

Storm tracks (e.g. Hollingsworth et al., 1996) on Mars are illustrated in Fig. 4, which depicts time-averaged (over 10 Ls) eddy amplitudes at ~ 1 km above the ground and highlights zonal asymmetries. At Ls 180, a local maximum in eddy activity is found in Utopia Planitia (longitude 120 E), whereas a minimum occurs over the Tharsis plateau (240 E). In the Southern Hemisphere, wave activity is deflected northward around the Hellas (30 E) and Argyre (300 E) basins. We note that at this time, SH eddy activity is stronger than the NH, a point we further explore in this work in Section 3.2. At Ls 270, lee cyclogenesis downstream of

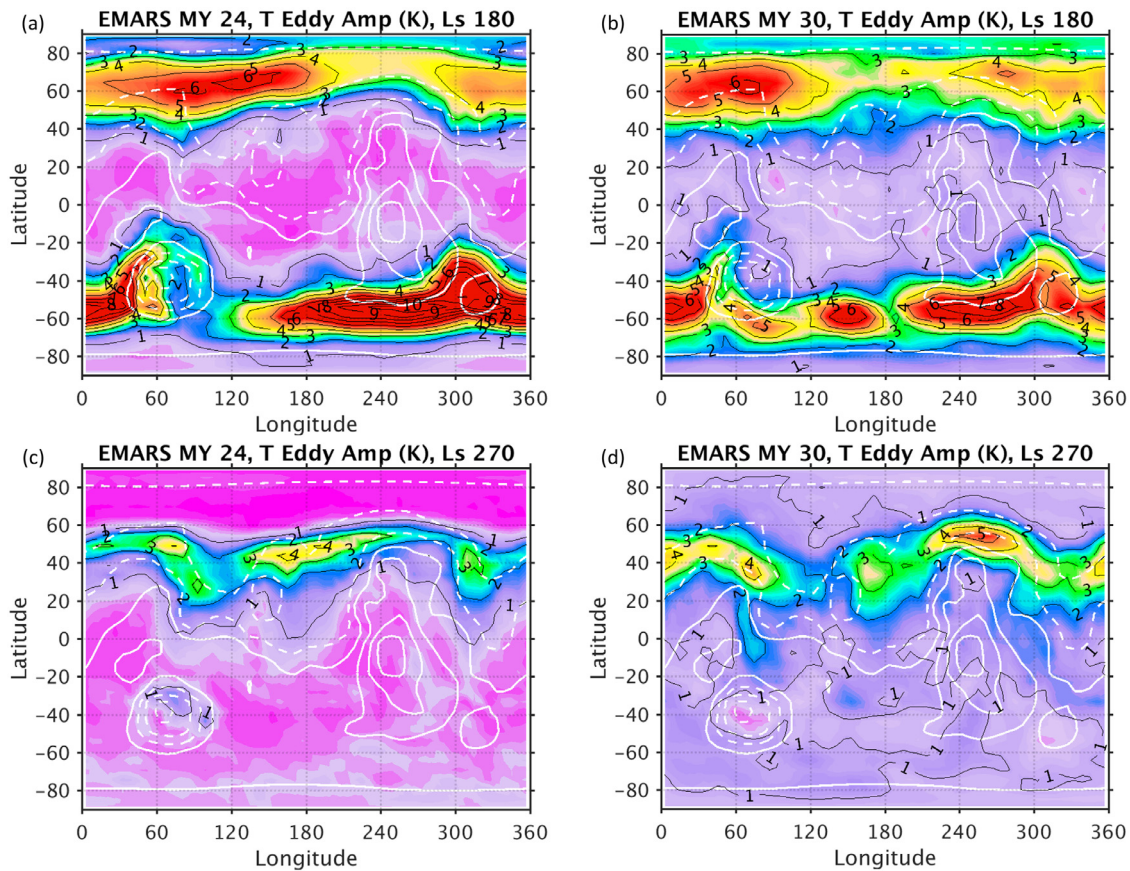


Fig. 4. Horizontal time-averaged (over 10 Ls) temperature [K] eddy amplitudes for EMARS at the model sigma level ~ 1 km above the surface for MY 24 (a, c) and MY 30 (b,d) at Ls 180 (a,b) and Ls 270 (c,d), which reveal the location of “storm tracks”. White contours indicate surface elevation at 2 km intervals; dashed contours are negative heights.

Tharsis at Chryse Planitia (320 E) is evident.

3.2. Interannual variability of transient eddies

In order to place a discussion of interannual variability of transient eddies into context, it is first relevant to examine the interannual variations in the zonal mean temperature base state, as well as dust storm activity across the TES and MCS era. A zonal mean base state at Ls 180 is created by averaging together the temperature fields from the 3 TES

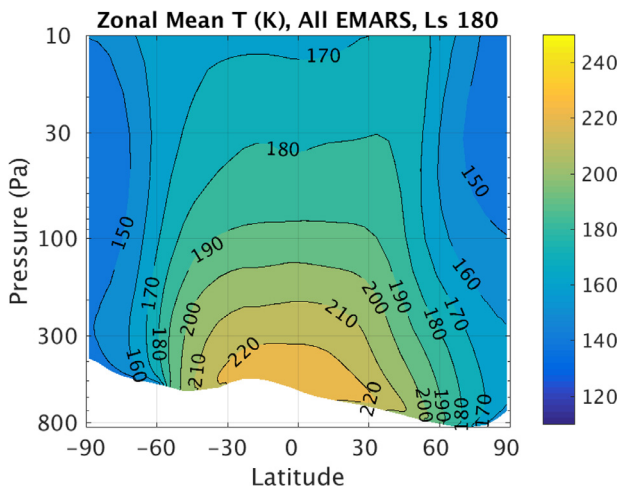


Fig. 5. EMARS zonal mean temperature [K] base state, averaged from Ls 175–185, as a mean across 6 Mars years: 24, 25, 26, 29, 30 and 31.

and 3 MCS years (Fig. 5). Fig. 6 depicts the difference between individual EMARS years and that zonal mean climatological base state. One year stands out as being particularly different, especially in the polar regions (MY 26). This is due to systematic errors with the TES observations which are most notable at low temperatures (Pankine, 2015; 2016); which is relevant because the temperature base state has a significant impact on transient eddies. MY 24 and 25 are in close agreement; this is just prior to the initiation of the global dust storm at Ls 185 in MY 25, after which they diverge. Likewise, the MCS years show relative agreement to within ~ 5 K; MY 29 experienced enhanced dust activity prior to this time (as shown below), and therefore has a warmer lower atmosphere. Fig. 7 depicts the zonally-averaged equatorial dust column optical depth across several Mars years. Dust activity is quietest between Ls 60 and 120. The MY 25 dust storm, which starts around Ls 185, shows the largest optical depths. MY 29 exhibits unusually early dust activity beginning around Ls 140, as well as a large regional dust storm at Ls 240. Of particular note are periods of elevated dustiness around Ls 220–240 and Ls 310–330, the “A” and “C” dust storm periods in the classification of Kass et al. (2016); these are indicative of cross-equatorial dust storms, whose origins are connected to transient eddies (e.g. Wang et al., 2003; 2005; 2013).

A six year climatology of transient eddy activity is presented, spanning both TES and MCS eras, and revealing similarities and differences. Fig. 8 depicts temperature eddy amplitude as a function of latitude and season, separately for each hemisphere. Throughout the period, transient eddies are found in each hemisphere during their respective autumn, winter, and spring seasons. During the winter solstice, a relative minimum in eddy activity is observed; this phenomenon has been referred to as the solstitial pause (Lewis et al., 2016; Mulholland et al., 2016). Maximal low-level eddy activity follows the waxing and

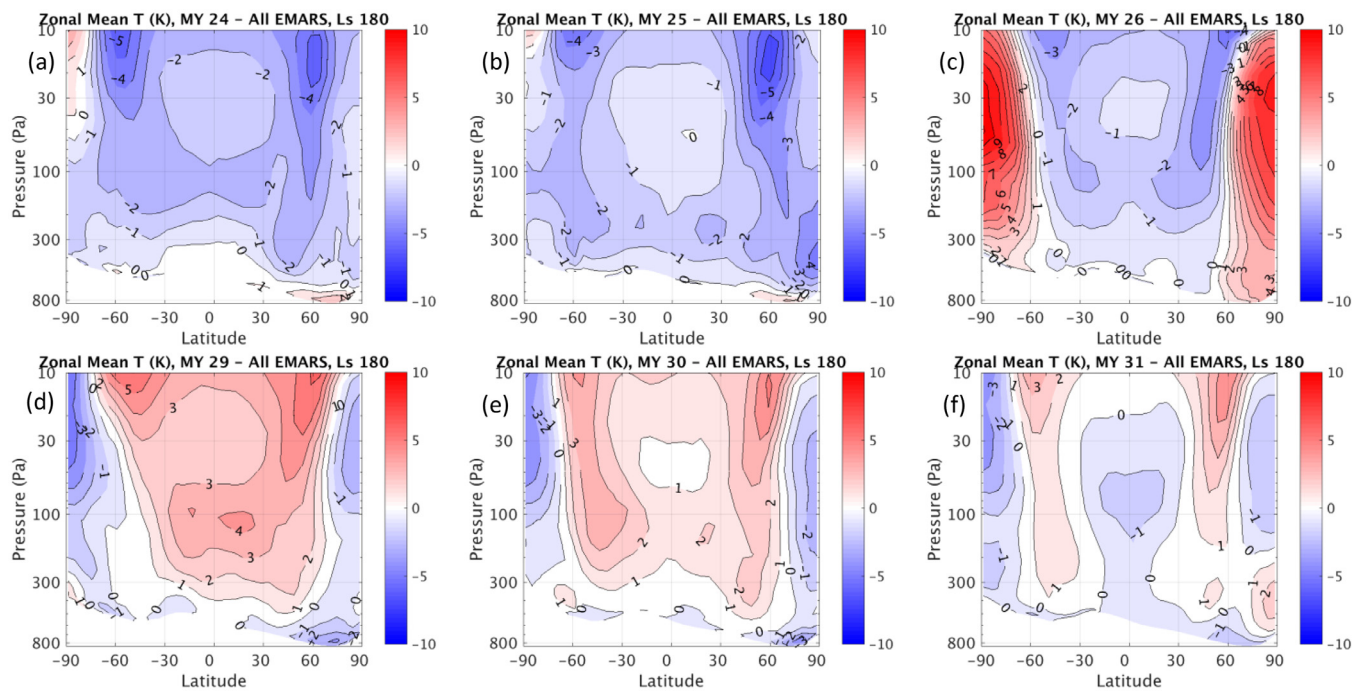


Fig. 6. Differences in EMARS zonal mean temperature [K] between a 6-year average and individual years for (a) MY24, (b) MY25, (c) MY 26, (d) MY 29, (e) MY 30, and (f) MY 31. Each plot features data averaged from Ls 175–Ls 185.

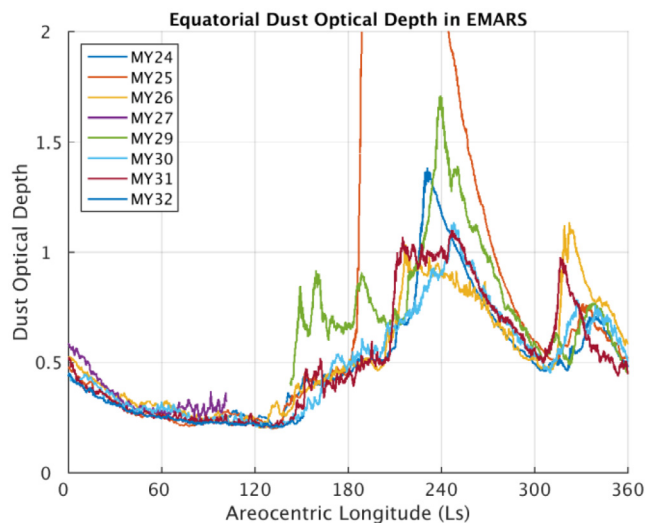


Fig. 7. Zonally-averaged equatorial dust column optical depth across Mars Years 24–27 and 29–32 from EMARS, which is guided by the Montabone et al. (2016) dust scenarios.

waning of the seasonal CO₂ polar cap edge (as shown in Mooring and Wilson, 2015), as the waves feed off the baroclinic instability generated by the associated temperature gradient.

Next, interannual variability is assessed. Mars year 24 and 26 present a good point of comparison for NH interannual variability during the TES era (Fig. 8a, c), with eddy activity peaking around 7 K in the northern hemisphere. Mars year 25 featured a global dust storm (initiated around Ls 185; Strausberg et al., 2005), and therefore has somewhat suppressed eddy activity due to stabilization and reduced baroclinicity during times of large dust opacities (e.g. Battalio et al., 2016). Noted are several periods with missing observations, for example MY 25 Ls 320 and MY 29 Ls 330 when eddy amplitudes appear artificially reduced; we further address this point in Section 3.4. The apparent interannual variability in eddy amplitude between MY 26 and

MY 24/25 is most likely due to the TES temperature issues in MY 26 that result in an anomalously warm SH polar region (see Fig. 6). EMARS during the MCS period (Fig. 8b, d) has little interannual variability in total eddy amplitude between MY 29, 30, and 31.

We next explore several systematic differences in eddy amplitudes and seasonality between the 3 EMARS TES years and the 3 EMARS MCS years. The traveling wave season in the SH extends considerably further for MCS (through Ls 240) compared to TES (ending before Ls 210). Eddy amplitudes as assimilated from the MCS observations are generally weaker in the NH (peak amplitudes of 5–6 K) compared to those assimilated from TES; whereas the TES traveling waves are clearly stronger in the NH compared to the SH (except around Ls 180), the amplitudes are of a closer size for MCS. There is greater temperature variability in the tropical regions for MCS compared to TES. Finally, the solstitial pause is less pronounced in MCS EMARS. It is unlikely that the real Mars atmosphere eddies have systematically different behavior in the first 3 years versus the later 3 years. Therefore, it is important to consider differences in the observing system, model, and assimilation system to explain the differences. We note that the exact length of the SH eddy season is an open scientific question; whereas early studies based on TES observations indicated a weakening by around Ls 200, the observations of front-like dust storms in Wang et al. (2011) in the SH around Ls 220 provide possible observational evidence that storms can last this late in the year. To provide additional helpful information, we have added the model simulated seasonal CO₂ ice cap edge to Fig. 8; this indicates the baroclinic zone where the transient eddies are found. The SH transient eddies generally follow this cap edge through Ls 240 for the MCS results. We note that model eddy activity (both amplitude and seasonality) is sensitive to the zonal mean temperature state of a model and its aerosol distribution (Mulholland et al., 2016; Lee et al., 2018); these papers show model simulations with extended SH eddy seasons. The addition of radiatively active clouds to model simulations increase eddy amplitudes (e.g. Pottier et al., 2017). MCS and TES observations disagree on the amount of aerosol near the polar cap edge (Montabone et al., 2015); we examined free run simulations for both the TES and MCS dust distributions and found slight enhancements to late SH dust activity, although insufficiently large to explain the

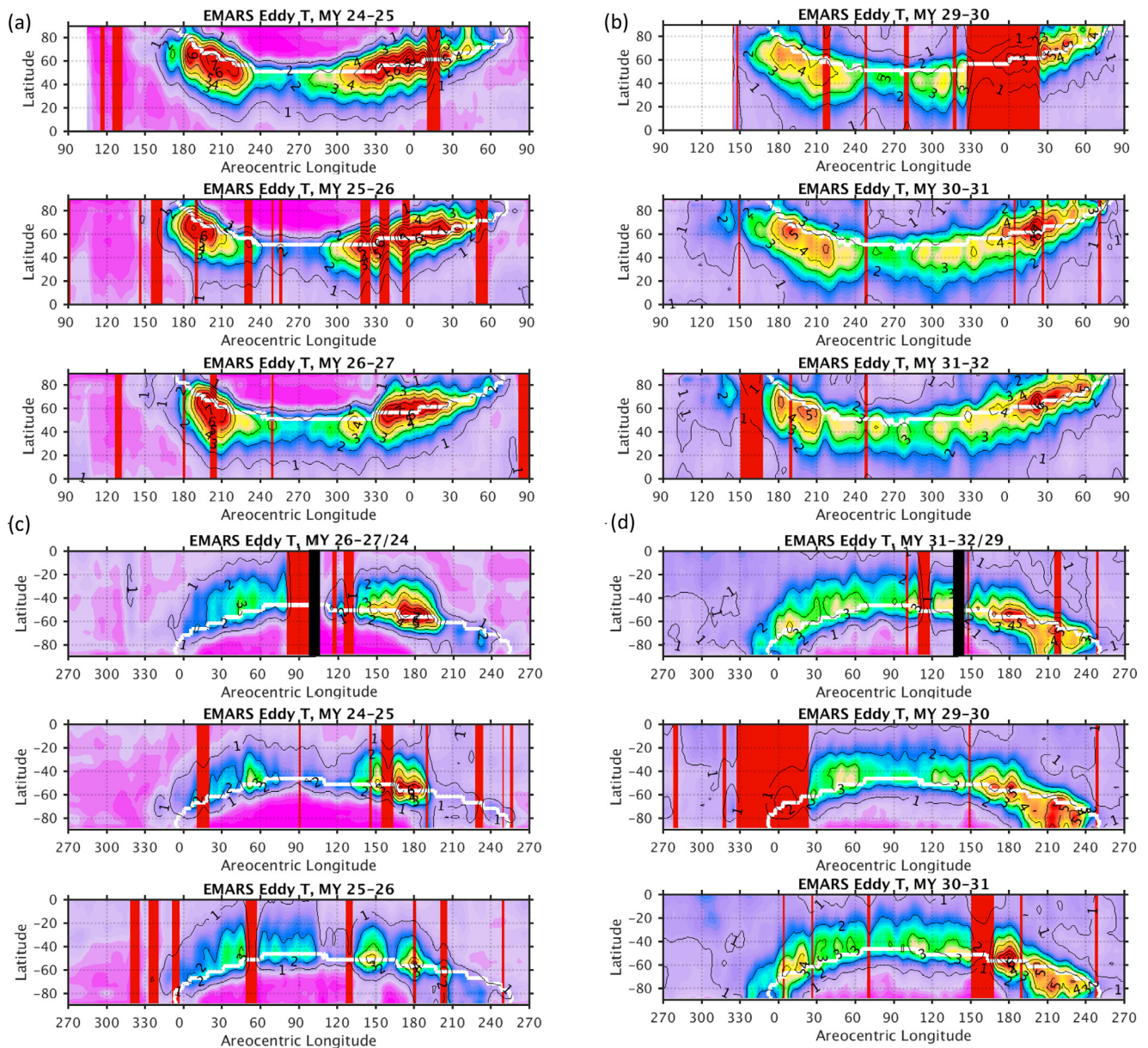


Fig. 8. EMARS Northern (a, b) and Southern (c, d) Hemisphere Temperature eddy wave activity (RMS amplitude, K) for (a, c) MY 24–26 (TES era) and (b, d) MY 29–31 (MCS era) at the model sigma level ~ 1 km above the surface. Thick red bars over the plots indicate time periods when spacecraft observations were not available. Vertical black bars in (c) and (d) indicate a discontinuity in time in the plots due to the ends of the EMARS reanalysis period. White lines indicate modeled location of seasonal CO_2 ice cap edge. (For interpretation of the references to color in this figure legend, the reader is referred to the web version of this article.)

systematic differences in EMARS. Therefore, the instrument characteristics may play a greater role, which we elaborate upon more deeply in the next section. To further explore interannual variability of Martian weather, eddy activity will next be analyzed by wavenumber.

3.3. Wave Regimes and reanalysis intercomparisons

The existence of wave regimes in EMARS is explored by analyzing eddy amplitude by wavenumber. Fig. 9 shows temperature eddy energetics for wavenumbers 1, 2, and 3 for MY 24 (representative of the TES era) and MY 30 (representative of the MCS era), which correspond to the respective panels in Fig. 8. Amplitudes for each wavenumber vary between 1 and 5 K (during the seasons which waves are present), with zonal waves 2 and 3 having a slightly higher amplitude than zonal wave 1. Wave amplitudes during the TES period appear somewhat larger than those during the MCS period. Although at a given time eddy energy is divided among 3 wavenumbers, one can characterize a wave

regime by the wavenumber with the maximal temperature variance. For example, in MY 24 wave 3 dominates around Ls 225, a time when cross-equatorial dust storms have been documented to occur (Cantor et al., 2001, 2007).

Transient eddies in two reanalyses (EMARS and MACDA) can be demonstrated to be more similar to one another than to the individual freely-running models. Figs. 10b and 11b show the wave energy climatology of a freely running GFDL MGCM simulation (NH and SH, respectively), configured similar to EMARS but without assimilating any observations. The model wave climatology is distinct from EMARS (Figs. 10a, 11a). In the NH, the control run has larger eddy temperature amplitudes, a stronger zonal wave 2, and a less distinct solstitial pause. In the SH for the control run, waves are stronger during the transition seasons, but weaker or absent during the peak of SH winter. Eddies in MACDA (Figs. 10c and 11c) and its control run (Figs. 10d and 11d) are also quite distinct (see also Mooring and Wilson, 2015). The UK control run lacks a NH solstitial pause, and has very weak SH eddy amplitudes

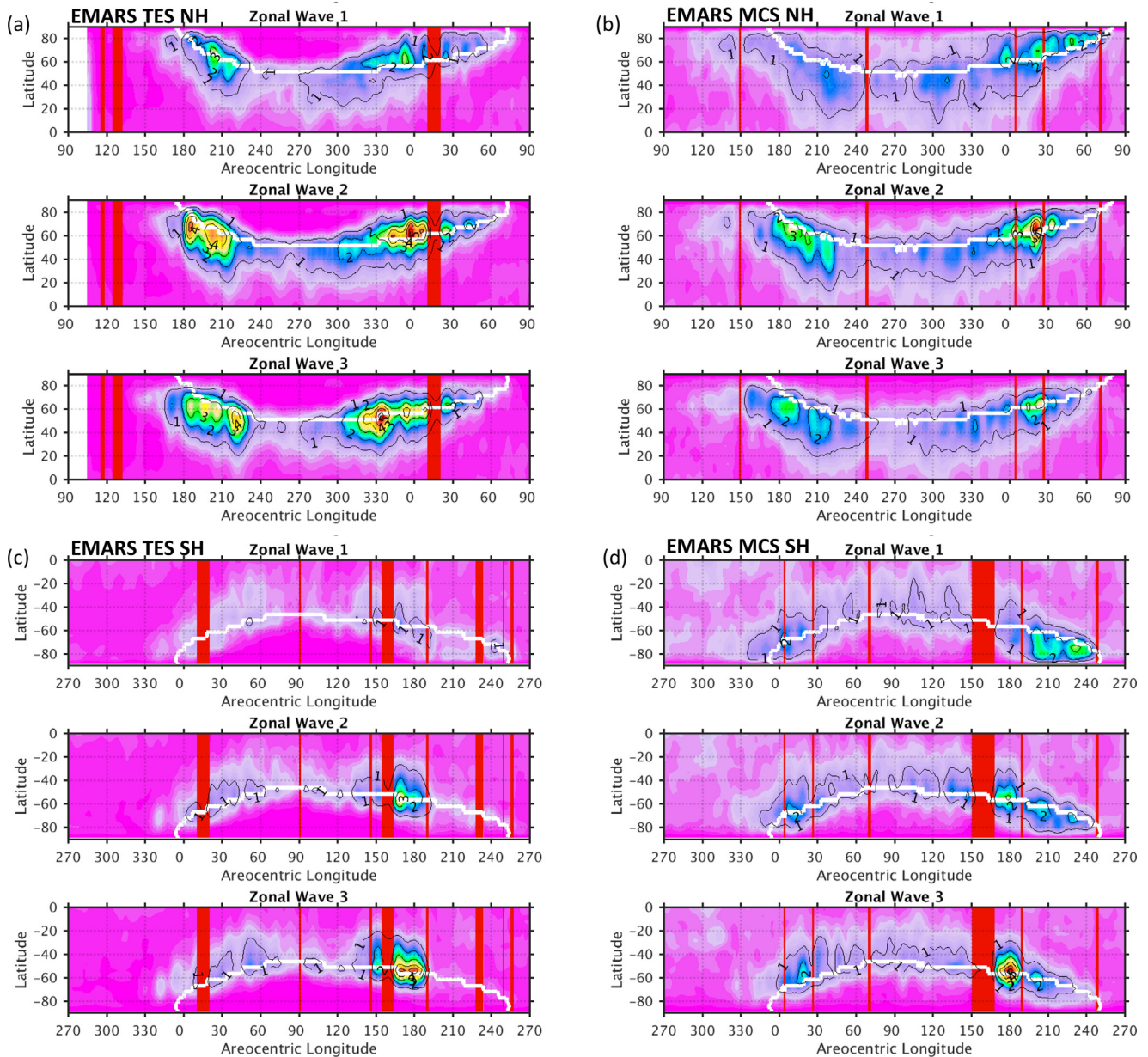


Fig. 9. EMARS Northern (a, b) and Southern (c, d) Hemisphere Temperature eddy wave activity contributions by zonal wavenumbers 1–3 for (a, c) MY 24/25 (TES era) and (b, d) MY 30/31 (MCS era) at the model sigma level ~ 1 km above the surface.

compared to MACDA. By contrast, the eddy amplitudes in MACDA and EMARS are of mainly similar amplitude and seasonality, both in total amplitude and among the various zonal wavenumbers. One notable exception is the SH wave 3 activity around Ls 150–180, which is stronger in EMARS than in MACDA; this may be related to the strength of the SH wave 3 in the respective GCMs, as the UK control simulation has very weak eddy activity in the SH.

Next we compare the amplitudes of transient eddies in a representative ensemble member (member 8, which has the median dust and water ice aerosol forcing; Fig. 12) with those of the ensemble mean analysis. We find that the individual member has similar eddy amplitudes to that of the ensemble mean for the TES era, whereas the amplitude (~ 8 K) of the individual member for MCS (assimilating along-track observations only) exceeds that of the ensemble mean (~ 5 K). MCS limb observations are limited within 5–10 km of the ground, both intrinsically by the limb geometry and the strong influence of aerosols,

which makes it difficult to constrain the shallowest waves. This indicates that for the TES reanalysis, the ensemble has converged about a unique synoptic state, whereas for the MCS reanalysis there is still some uncertainty about the structure and phase of lower atmosphere waves. This is further explored by plotting ensemble spread in the atmosphere; larger spread is found in the region of lower atmosphere transient eddies for MCS compared to TES (not shown). An additional means of assessing convergence is obtained through examining synoptic maps of the ensemble mean versus individual ensemble members (Fig. 13). Fig. 13a shows that all 16 ensemble members have largely converged about the ensemble mean (bottom right of the panel); members show a zonal wave 3 signature with similar phasing, and pressure eddy amplitudes of around 40 Pa. When the ensemble converges about its mean (and the spread / skill relationship is maintained), this is an indication that there is sufficient observational information to constrain the reanalysis about a unique synoptic state. When waves of similar

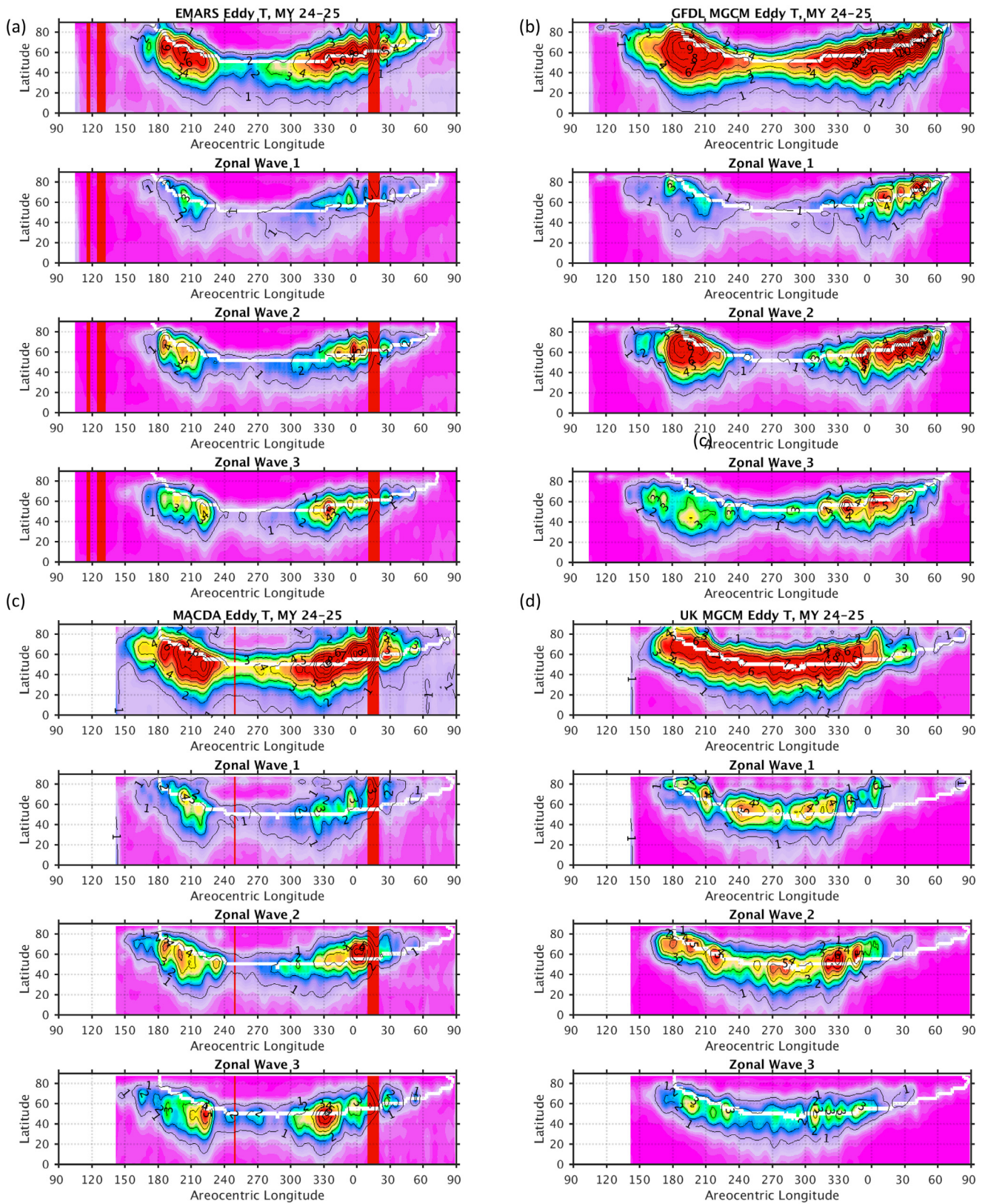


Fig. 10. (a) EMARS and (b) the corresponding GFDL MGCM control run with (c) MACDA and (d) the corresponding UK MGCM control run for Northern Hemisphere eddy temperature [K] wave activity: total RMS amplitude (top row) and by zonal wavenumber (next 3 rows) for MY 24/25 (TES era) at the model sigma level ~ 1 km above the surface. UK MGCM control run courtesy of MACDA team; see acknowledgments for further details.

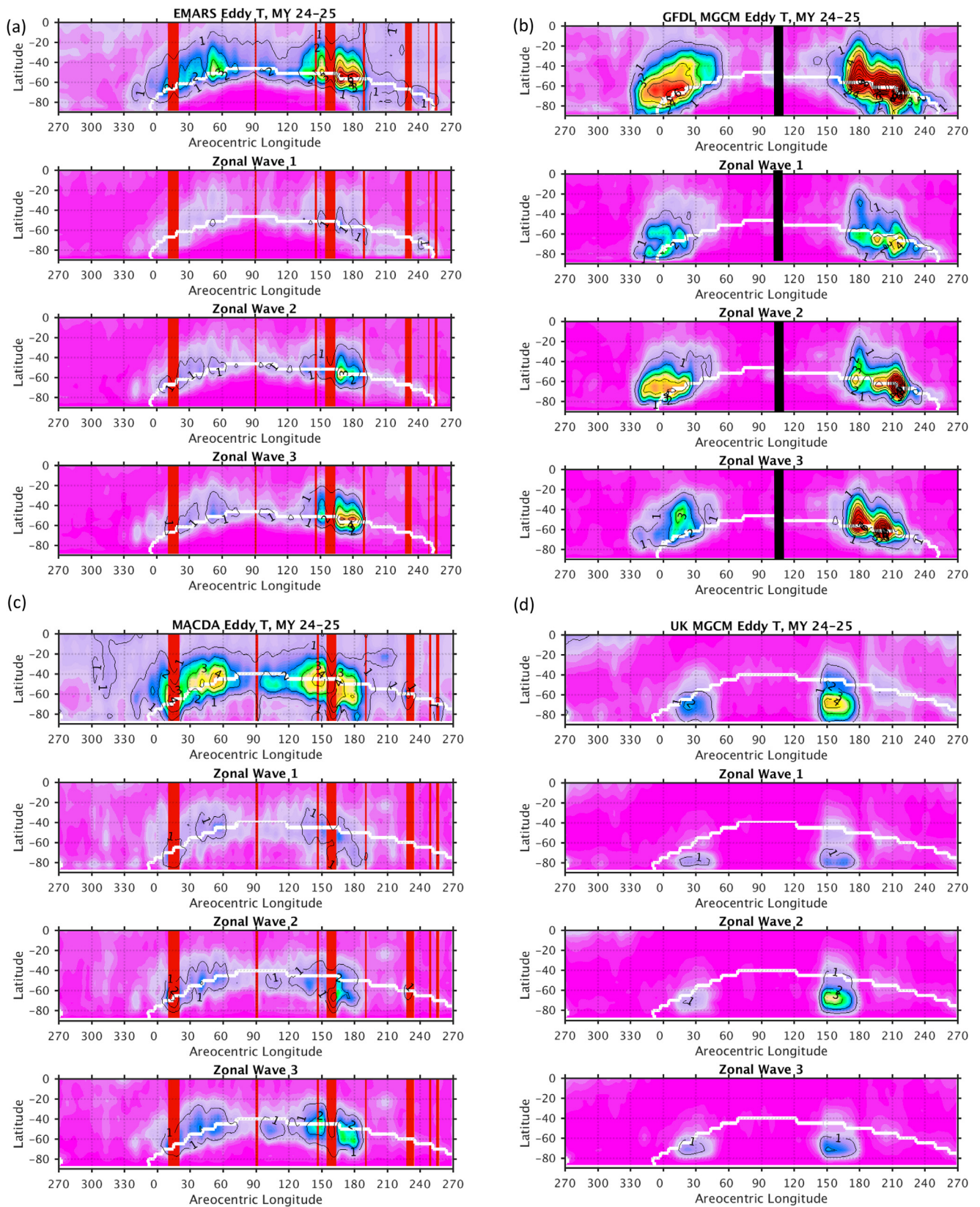


Fig. 11. (a) EMARS and (b) the corresponding GFDL MGCM control run with (c) MACDA and (d) the corresponding UK MGCM control run for Southern Hemisphere eddy temperature [K] wave activity: total RMS amplitude (top row) and by zonal wavenumber (next 3 rows) for MY 24/25 (TES era) at the model sigma level ~ 1 km above the surface. White lines indicate modeled location of seasonal CO₂ ice cap edge for each respective product. The black bar in (d) denotes a jump in time from Ls 105 in MY 25 to Ls 105 in MY 24. UK MGCM control run courtesy of MACDA team; see acknowledgments for further details.

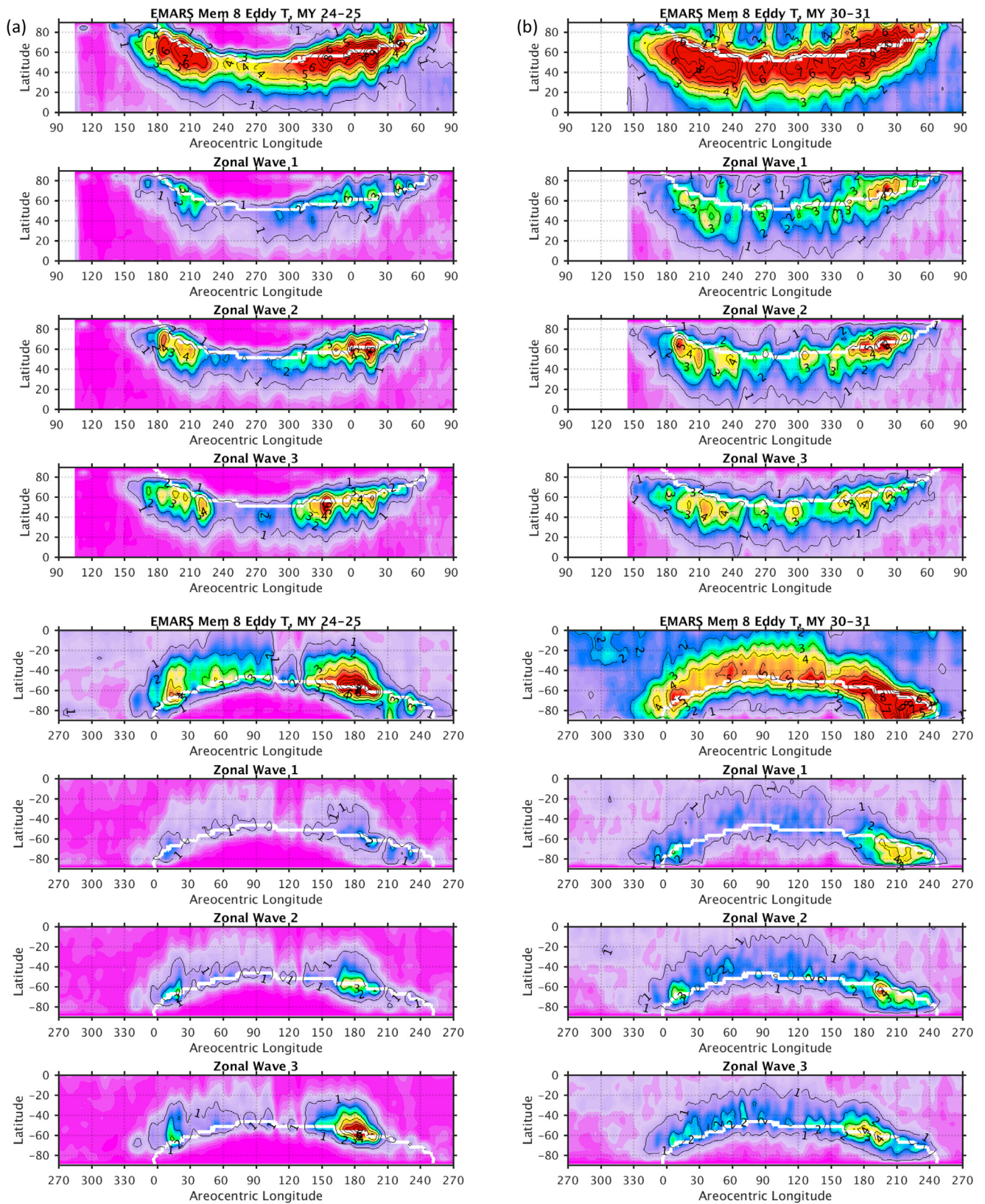


Fig. 12. EMARS ensemble member 8 for (a) MY 24/25 and (b) MY 30/31 along-track MCS Northern Hemisphere temperature (K) eddy wave activity: total RMS amplitude (top row) and by zonal wavenumber (next 3 rows) at model sigma level ~ 1 km above ground.

amplitudes but somewhat different phases are averaged together, the resulting ensemble mean state has a weaker amplitude. This weaker degree of convergence is evident in Fig. 13b for the MCS EMARS; whereas the mean shows some general features in agreement (such as

the cold phase of an eddy near longitude 90, and a general wave 3 pattern), the individual members show significant variability in the location of the strongest eddy amplitudes and the structure, in particular for the pressure field. We consider the ensemble nature of EMARS

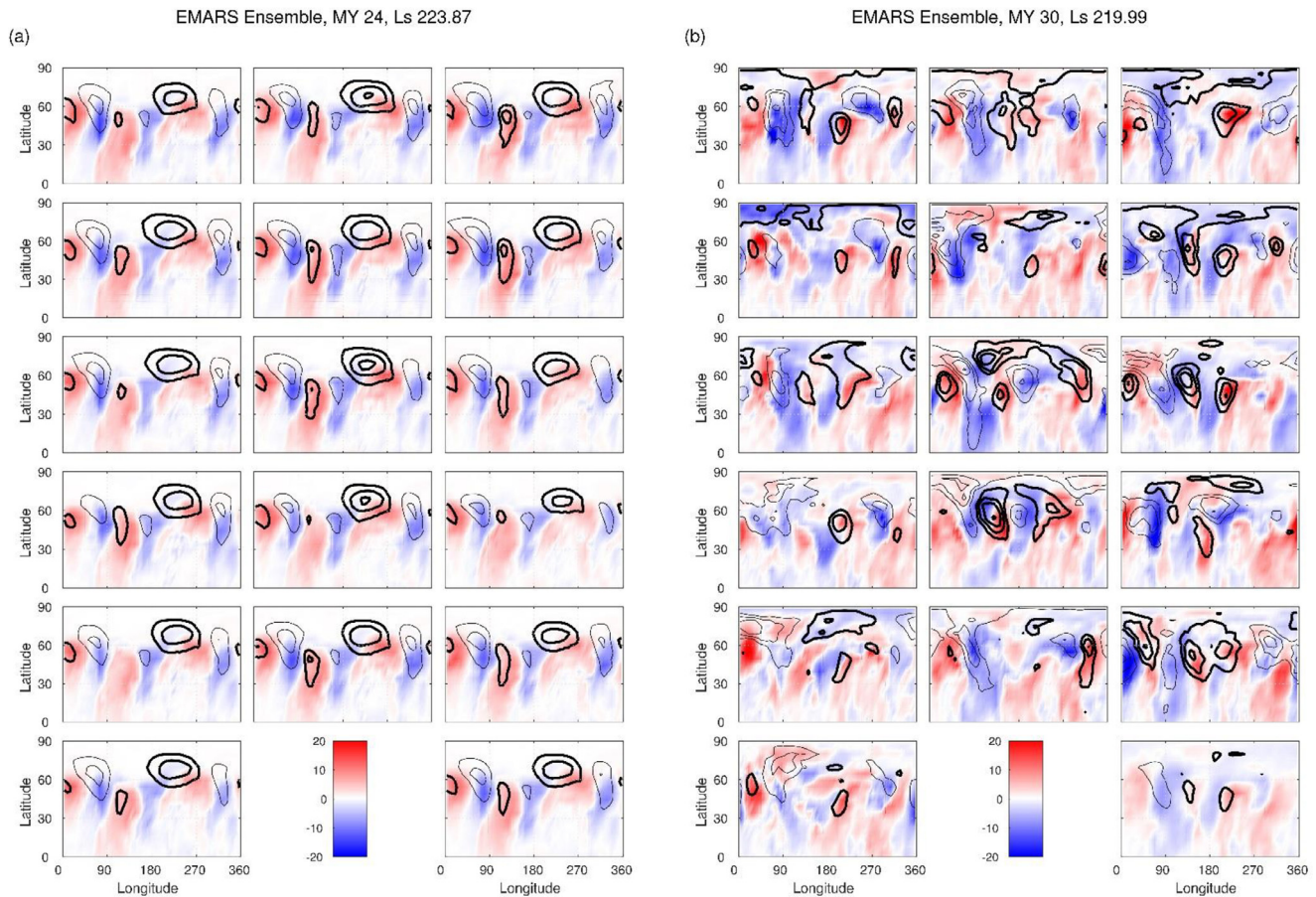


Fig. 13. Synoptic maps of every ensemble member in EMARS while assimilating (a) TES observations and (b) MCS along-track observations, with the ensemble mean at bottom right, at the same times as the synoptic maps in Fig. 1. Temperature eddy amplitude is shown in color, with full saturation being a 20 K eddy amplitude. Pressure eddy amplitude is contoured at 20 Pa intervals, with low pressure bolded. Ensemble members have increasing dust downwards and increasing ice radiative forcing rightwards.

as a strength: the ensemble mean shows the most likely wave phase, the ensemble spread shows the uncertainty in the wave position, and an individual ensemble member provides representative wave amplitudes. Whereas the deterministic MACDA provides a representative wave amplitude, it does not provide any information on the confidence of the assessment of the wave phase or amplitude. Fig. 14 depicts the observation density by latitude and longitude for MCS, note the reduced observation counts in the dayside equatorial cloud belt and near the winter polar vortex. This difficulty in sensing the lowest few km by MCS where the shallow eddies reside may be one of the reasons for the lack of strong convergence about a unique atmospheric state. By contrast, nadir TES observations have sensitivity to the lower atmosphere, although they exhibit a high degree of vertical smoothing.

Wave regimes across several Mars years are explored to see whether a given wavenumber tends to be favored during certain seasons. Fig. 15 summarizes the dominant wave regimes in both EMARS and MACDA by finding the zonal wavenumber with the largest amplitude across all latitudes in each hemisphere. During the TES era, the amplitudes of waves 2 and 3 tend to be the largest (wave 1 is also present, just not as dominant). For example, in the NH wave 3 is present in both reanalyses at MY 24 Ls 225 and MY 24 Ls 310–335, among other periods. Eddy activity lasts from around Ls 150 to Ls 60 in the NH, and Ls 0 to Ls 190 in the SH; during the intervening summer periods eddy amplitudes are too weak to be categorized into wave regimes. One can also compare wave regimes between the TES and MCS eras. The spring season seems to favor wave 3 activity (for example, at Ls 315 wave 3 is found in 5 years of reanalyses for the NH; at Ls 180 it is found in all 6 years of reanalyses). Wave 2 is favored more in autumn (at Ls 190, wave 2 is

found in all 6 years of reanalysis for the NH; at Ls 10 it is found in 5 of 6 years of reanalyses). While the wave regime does not appear to be exactly repeatable from season to season, there is a preferred seasonality to the regimes. There is also some evidence of agreement in wave regime characterization between EMARS and MACDA.

3.4. Robustness of waves to model and assimilation changes

A significant milestone in the development of atmospheric reanalyses for Mars is a demonstration that reanalyses converge upon the “true state” of the Martian atmosphere, and differences from model and assimilation configuration are smaller than that of analyses versus free run (Greybush et al., 2012). This would give confidence that the reanalyses are not simply showing the transient eddy state of the underlying GCM, but rather are being driven by the observations toward the eddy states actually observed at specific times and locations. One way to accomplish this is the comparison of Hovmöller diagrams (which show eddies as a function of time and longitude) for EMARS, MACDA, and a freely running MGCM. Fig. 16 is a northern hemisphere temperature eddy Hovmöller diagram during the NH autumn (Ls 180–240), an active time for transient eddies. As waves have a similar phase speed as they travel west to east, the spacing of the peaks and troughs (warm and cool) gives an indication of the dominant wave regime; wave 3 features a characteristic ~ 2 sol period, whereas wave 1 has peaks and troughs spaced further apart with a period of ~ 6.7 sols. There is a clear distinction between the two reanalyses and the MGCM control run; the latter has more regular waves with somewhat larger amplitudes. The reanalyses feature waves with more variety in

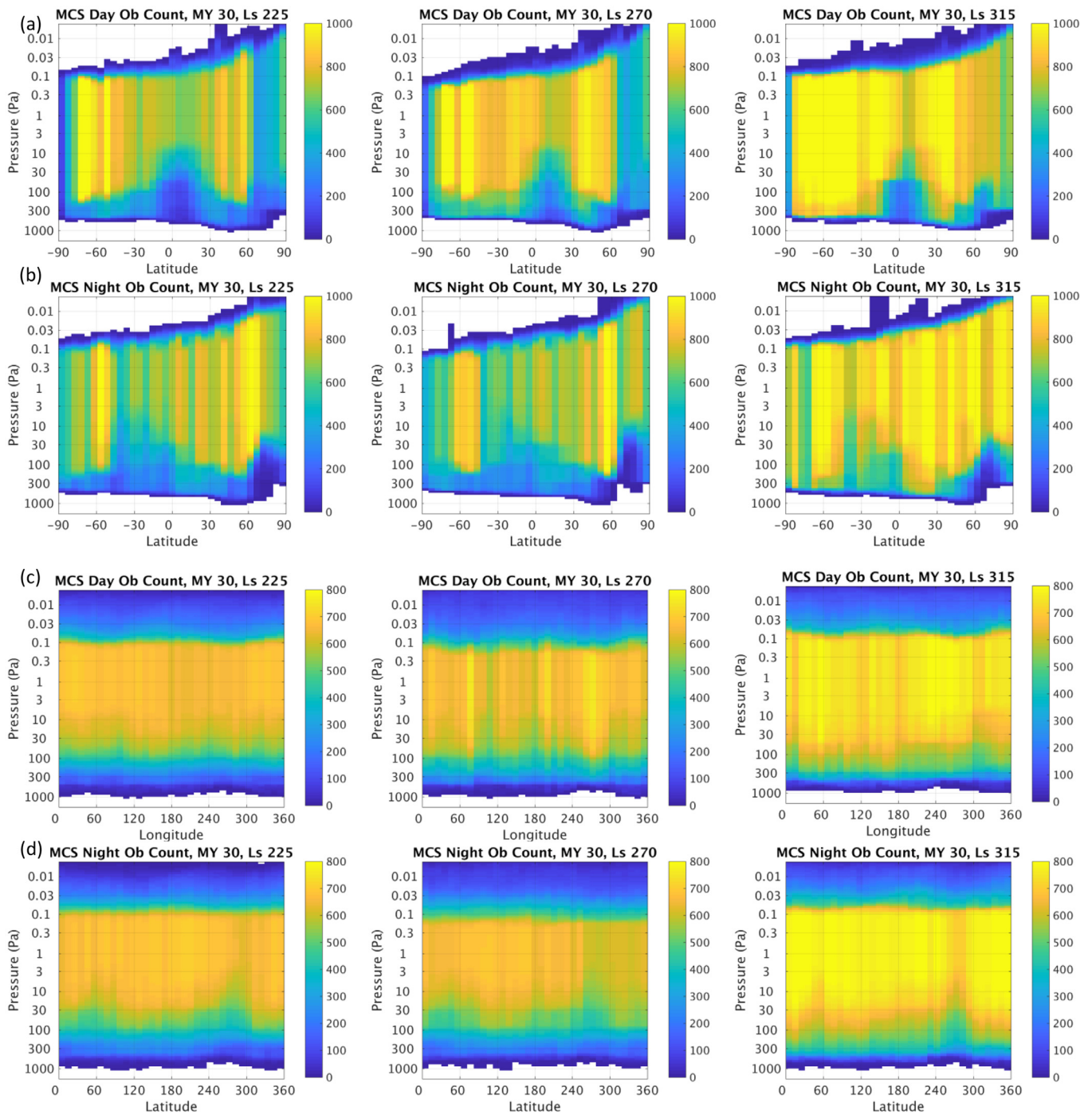


Fig. 14. MCS retrieval observation counts during the (a, c) daytime and (b, d) nighttime as a function of (a, b) latitude and (c, d) longitude and pressure, for the 10 Ls period centered around MY 30 Ls 225, 270, and 315.

wavenumbers. They also see a general agreement in phase of the wave; for example, one may trace the wave starting at longitude 0° at Ls 200, Ls 205, or Ls 225 in both reanalyses. MACDA has a stronger zonal wave 3 than EMARS at Ls 220–238, the time of a regional dust storm. Comparisons of animated synoptic maps also show that EMARS and MACDA generally have waves with similar phasing. The agreement between two eddy fields can be quantified using the anomaly correlation metric, long used to evaluate the performance of NWP models for the Earth.

It is important to understand the sensitivity of transient eddies to

the underlying assumptions used in the model and data assimilation system. One way of assessing this sensitivity is comparing EMARS and MACDA directly; they averaged an anomaly correlation of 0.58. This contrasts with the much lower value of -0.03 between EMARS and its control run. Another method is by generating short, alternate reanalyses (during MY 24 NH autumn) with the EMARS system, but using different assumptions in the underlying MGCM simulation or in the LETKF assimilation scheme: turning off the radiatively active water ice clouds (the current version of MACDA does not have radiatively active clouds), removing the filter for temperature observations below the CO₂

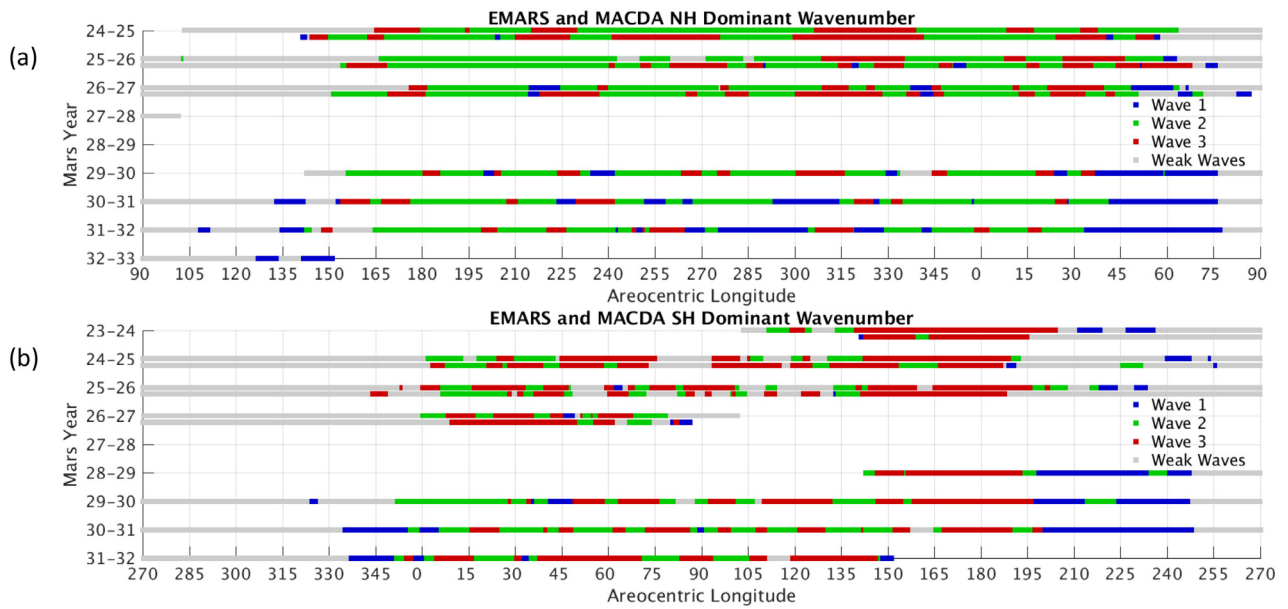


Fig. 15. Wave regime diagram for the (a) northern hemisphere and (b) southern hemisphere. The maximum zonal mean eddy amplitude, for each hemisphere, time, and wavenumber, is computed. The wavenumber with the greatest eddy amplitude is shown, unless that eddy amplitude is less than 1 K. During the TES era, the EMARS and MACDA reanalyses are plotted in pairs, with EMARS on top and MACDA on the bottom.

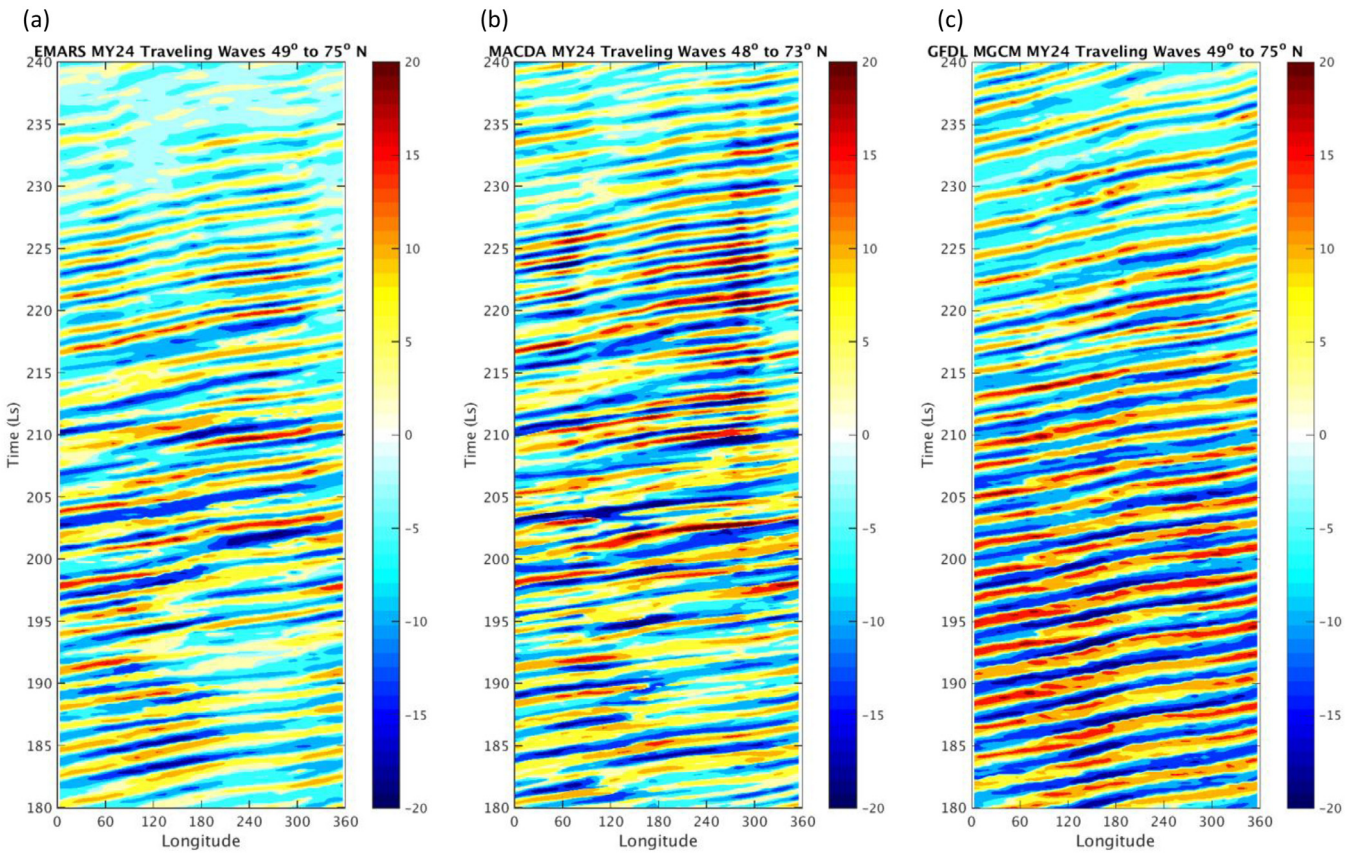


Fig. 16. (a) EMARS, (b) MACDA, and (c) EMARS MGCM control run NH temperature eddy Hövmler diagram for MY 24 (TES era) Ls 180–240, using the maximum eddy amplitude between latitudes 49–75 N.

critical temperature, and replacing the vertical averaging in the forward operator with a simple interpolation. A final experiment assimilates TES temperatures only at levels above 500 Pa; this was intended to approximate the reduced sensitivity to the lowest levels of the atmosphere found in the MCS observations, and investigate the impact of MCS

vertical observational availability to explain the systematic difference between reanalyses based on MCS and TES observations. These results are summarized in Table 1. Recall that anomaly correlation of 1 would be a perfect pattern match, with skill decreasing for values less than one. The transient eddy states in alternate versions of EMARS had the

Table 1

Table of anomaly correlation statistics comparing temperature eddies in EMARS with its control run, MACDA, and alternate runs of EMARS. The characteristics of these alternate runs are also specified in the table.

Assimilation run	Anomaly correlation	Radiatively active water ice clouds	CO ₂ critical temperature filter	Level-weighting forward operator	Observations assimilated
EMARS MGCM control	−0.0346	Yes	N/A	N/A	None
MACDA V1.0	0.5766	No	Yes	Yes	TES
Alt EMARS: noTcrit	0.8471	Yes	No	Yes	TES
Alt EMARS: nolowerT	0.5720	Yes	Yes	Yes	TES only above 500 Pa
Alt EMARS: noclouds	0.8396	No	Yes	Yes	TES
Alt EMARS: wsingle	0.7812	Yes	Yes	No	TES
Alt EMARS: wsingle_noTcrit	0.8139	Yes	No	No	TES

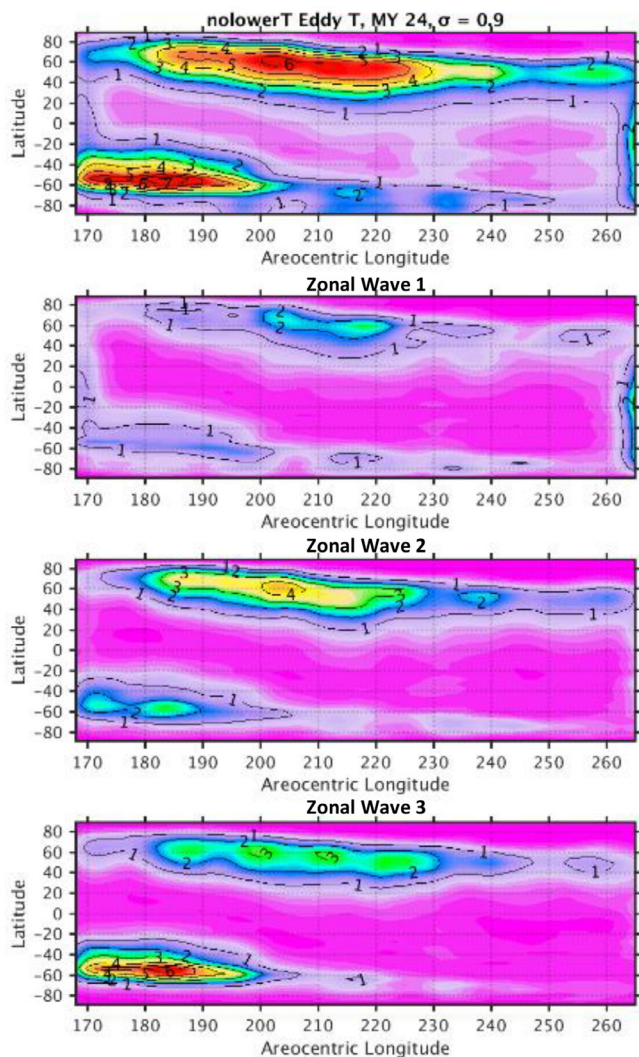


Fig. 17. Eddy temperature amplitude and wavenumber decomposition as a function of latitude and season for an alternate run of EMARS where TES temperatures are only assimilated at levels above 500 Pa.

smallest sensitivity to choice of critical temperature filter, forward operator, and water ice clouds, with anomaly correlations between these respective runs and the control run of around 0.8. Removing the lowest temperature observations had a more substantial impact, with anomaly correlations around 0.57. Fig. 17 shows that the wave amplitudes were reduced (in particular, for wave number 3) when removing these lower atmosphere observations; we also note that MCS reanalyses generally had smaller wave amplitudes than TES reanalyses which concurs with this result.

Another consideration is what happens to reanalyses during a gap in observations. During this time, the model simulations are unforced by observations, and begin to relax to the behavior favored by a freely running simulation, which is sensitive to 3-D variations in dust and water ice clouds. Both the eddies and the basic state are influenced by choice of aerosol descriptions used in the models. In the absence of data input, the reanalyses quickly (~couple of sols) relax back to a zonal mean temperature state consistent with the dust fields, which may be more or less conducive to supporting traveling waves. In the case of MACDA, the single “nudged” simulation generates a single realization of the estimated synoptic wave state, which may be different than the “true” state. In the case of EMARS, an ensemble of model simulations each drifts to their own wave state. Waves with different phases (and amplitudes) begin to destructively interfere with each other in the ensemble mean, and the eddy amplitude of the ensemble mean is reduced (see Fig. 13). This behavior can be seen in Fig. 8, with the reduced amplitudes of waves between MY 29 Ls 330 and MY 30 Ls 30 during an extended data gap. This wave decorrelation is present in MY 25 as well, and becomes manifest within a few sols. Note that during this time, individual members would maintain waves of amplitudes comparable to that of a freely running simulation (e.g. Figs. 10 and 11). The fact that the ensemble mean eddy amplitude is similar to (for TES), or less than (for MCS) that of the eddy amplitudes in individual members gives confidence about when observations provide sufficient constraint to often lock in to the “true” synoptic state for EMARS.

3.5. Comparisons to independent observations

Validation of transient eddy characteristics against independent observations is challenging for Mars in view of the relatively sparse set of independent observations. The surface pressure records from landers provide a unique opportunity to do so. A source of in situ observations of atmospheric pressure is the Curiosity rover. However, the Curiosity rover lies near the equator (5°S) where transient eddies are more challenging to detect due to their smaller amplitudes (Fig. 8; Haberle et al., 2018). By contrast, the Viking landers (VL) are in the northern hemisphere, and therefore their in situ surface pressure observations are more suitable for comparison of eddy features. Because Viking observations occurred during Mars Years 12 through 15 (and hence long before TES or MCS), they can only be compared in a climatological sense (assuming transient eddies have similar statistics from year to year, a topic being investigated in this paper). Nonetheless, the Viking dataset provides valuable constraints on the amplitudes of pressure eddies, as well as estimates of dominant wave regimes, which are inferred from a Fourier (spectral) analysis of the surface pressure time series. Fig. 18 shows peak eddy pressure amplitudes of ~9 Pa and ~24 Pa at Viking lander 1 (22.5°N) and 2 (48°N), respectively (with the notable exception of a brief period in MY 14 at VL1, to be discussed later). These amplitudes are within a few Pa of the peak eddy pressure amplitudes in EMARS in MY 24–27 at the grid points closest to the Viking lander locations. Peak pressure amplitudes are slightly higher for MACDA, at ~14 and ~27 Pa respectively. The peak amplitudes in

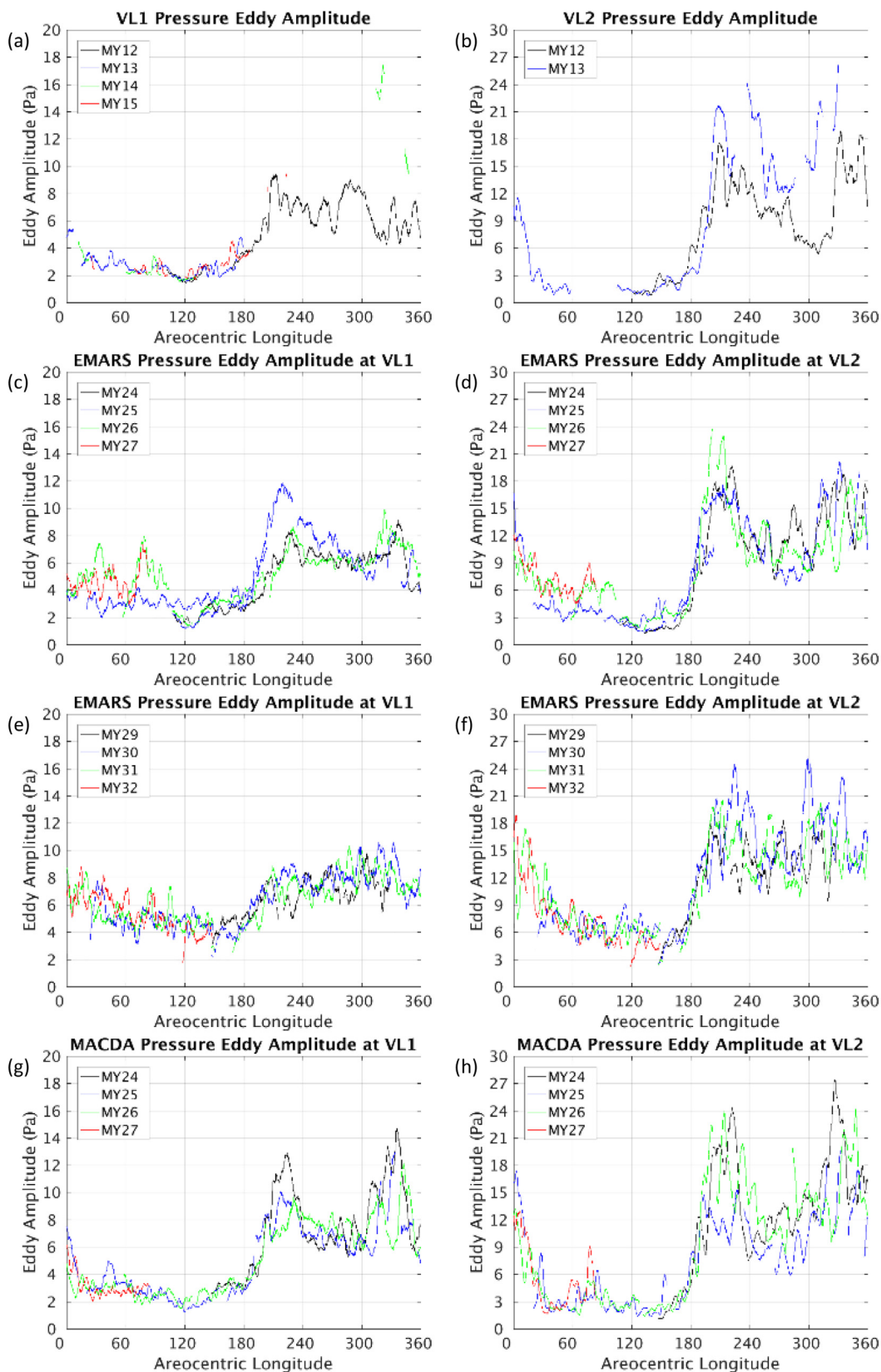


Fig. 18. Comparison of Viking surface pressure eddy amplitudes (Pa) at (a) VL1 (22.5°N) and (b) VL2 (48°N) during MY 12–15 (when available) along with EMARS surface pressure eddies sampled at the corresponding locations of VL1 and VL2 in MY 24–27 (c, d) and MY 29–32 (e, f) and MACDA during MY 24–27 (g, h).

EMARS in MY 30 are 10 Pa at Viking lander 1 and 24 Pa at Viking lander 2. This shows a relative agreement of Viking, EMARS (across TES and MCS periods), and MACDA with respect to pressure eddy

amplitude. There is also a key seasonal cycle, with a solstitial pause present in VL2 around Ls 270, and a quieting of waves during the NH summer. Both the solstitial pause and the quieting of waves are present

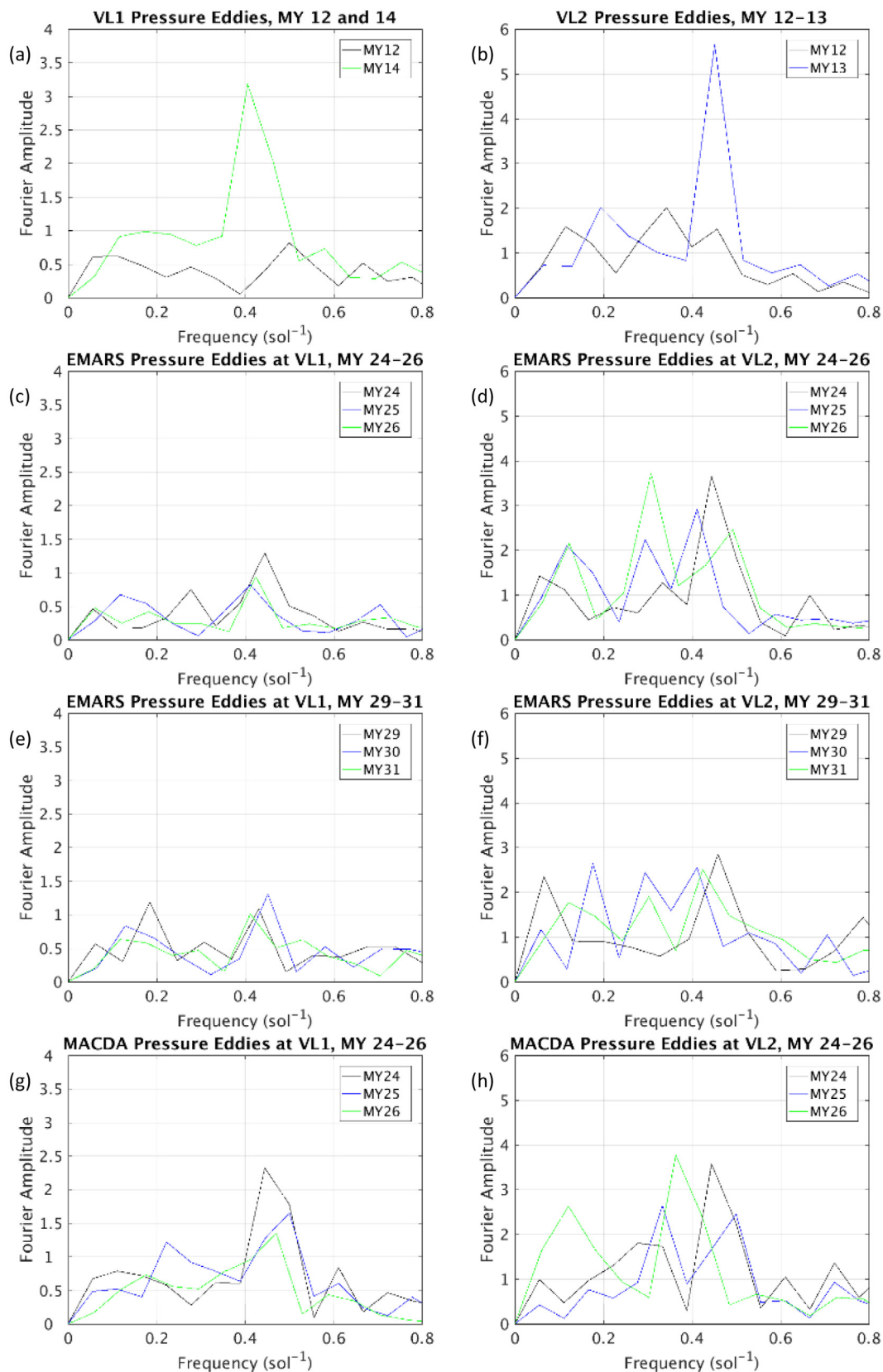


Fig. 19. Comparison of Viking surface pressure spectral signatures at (a) VL1 (22.5°N) and (b) VL2 (48°N) during MY 12–15 (when available) along with those from EMARS sampled at the corresponding locations of VL1 and VL2 in MY 24–27 (c, d) and MY 29–32 (e, f) and MACDA during MY 24–27 (g, h). Each curve has been selected to display the 10 Ls time period when the surface pressure Fourier amplitude in the 0.4 and 0.5 sol^{-1} frequency is maximized.

in the EMARS data, though the EMARS pauses (particularly for the MCS years) are less distinct than the Viking pauses.

Next, spectral signatures for a wave with a frequency of 0.4 to 0.5 sol^{-1} (or a ~ 2.3 sol period) were identified in both the observational and reanalysis datasets. This period wave is associated with zonal wavenumber 3 waves and with cross-equatorial “flushing” storm events (Wang et al., 2005). Fig. 19 shows the Fourier transform of Viking surface pressure data as well as pressure data from EMARS and MACDA nearest the Viking landers. Mars years 12–14 (based on data availability), 24–26, and 29–31 were chosen to represent Viking, the TES era, and the MCS era, respectively. The Ls bounds for the 10 Ls length periods analyzed in Fig. 19 (listed in Table 2) were chosen so that the peak amplitude of the 0.4 to 0.5 sol^{-1} wave was maximized; in other words, the strongest examples of waves with this period (2–2.5 sols) have been selected in each of the representative years and datasets. In all years at Viking lander 1, the maximum amplitude of the 0.4 to 0.5 sol^{-1} wave is between 0.6 and 3.2 (the latter being a likely strong cross-

Table 2

Description of the time periods selected for the spectral analyses plotted in Fig. 19 for each dataset (column 1) and Mars Year (column 2). Time periods (columns 3 and 4) were chosen so that the peak amplitude of the 0.4 to 0.5 sol^{-1} wave was maximized. Assume all time periods are of length 10 Ls centered on the reported value.

Dataset	MY	VL 1 Ls	VL 2 Ls
Viking	12	335	325
Viking	13	No Data	236.7
Viking	14	321	No Data
EMARS	24	335	335
EMARS	25	315	315
EMARS	26	305	205
EMARS	29	305	235
EMARS	30	225	315
EMARS	31	315	305
MACDA	24	335	335
MACDA	25	335	335
MACDA	26	315	195

equatorial storm); the EMARS and MACDA amplitudes fall within this range, with MACDA demonstrating slightly higher amplitudes than EMARS. At Viking lander 2, MY 13 has a strong wave with an amplitude of greater than 5, whereas activity in MY 12 is weaker (amplitude of 1.5). Wave amplitudes in the reanalyses fall between 2 and 4, which is again within the limits of interannual variability established by the observations.

The presence of this wave signature can be linked to dust storm activity. In MY 24, Ls 330–340 had the greatest 0.4 to 0.5 sol^{-1} wave amplitude at both Viking lander locations in EMARS and MACDA, and this time corresponds to the time leading up to the post-solstitial maximum in equatorial dust opacity in that year (Fig. 7). MY 30, Ls 310–320, the time of greatest 0.4 to 0.5 sol^{-1} wave amplitude at Viking lander 2, corresponds to a rapid increase in equatorial dust opacity (see Fig. 7). MY 30, Ls 220–230, the time of greatest 0.4 to 0.5 sol^{-1} wave amplitude at the location of VL1, corresponds to a period leading up to a minor maximum in equatorial dust opacity. Indeed, 14 out of 16 time periods listed in Table 2 during MY 24–30 also have a NH-originating dust storm observed by MOC or MARCI (Fig. 2 in Wang and Richardson, 2015). During the TES era, 9 of 12 of these times with maximum 0.4 to 0.5 sol^{-1} amplitude also saw a zonal wave 3 regime indicated in Fig. 15; the relationship was less clear for the MCS data with 2 of 6 times coinciding with a zonal wave 3.

We investigate the correspondence between zonal waves 1, 2, and 3 in EMARS and the prevalent wave periods of 6.7, 3.1, and 2.3 sols found in the Viking lander time series data by Barnes (1980). This correspondence between zonal wavenumber and period is supported by numerous MGCM studies (e.g. Kavulich et al., 2013) and observational studies. Fig. 20 shows a spectrogram created by first isolating the zonal wave 1, 2, and 3 components of the temperature eddy state from EMARS, and then taking the Fourier transform of the corresponding time series located at the latitude and longitude of Viking Lander 2. MY 24 was chosen to represent the TES era, while MY 30 was chosen to represent the MCS era; the major features of the spectrograms are similar among the other years in each respective era. In MY 24, most of the Fourier amplitude in zonal wave 1 was at 0.15 sol^{-1} , or period 6.7

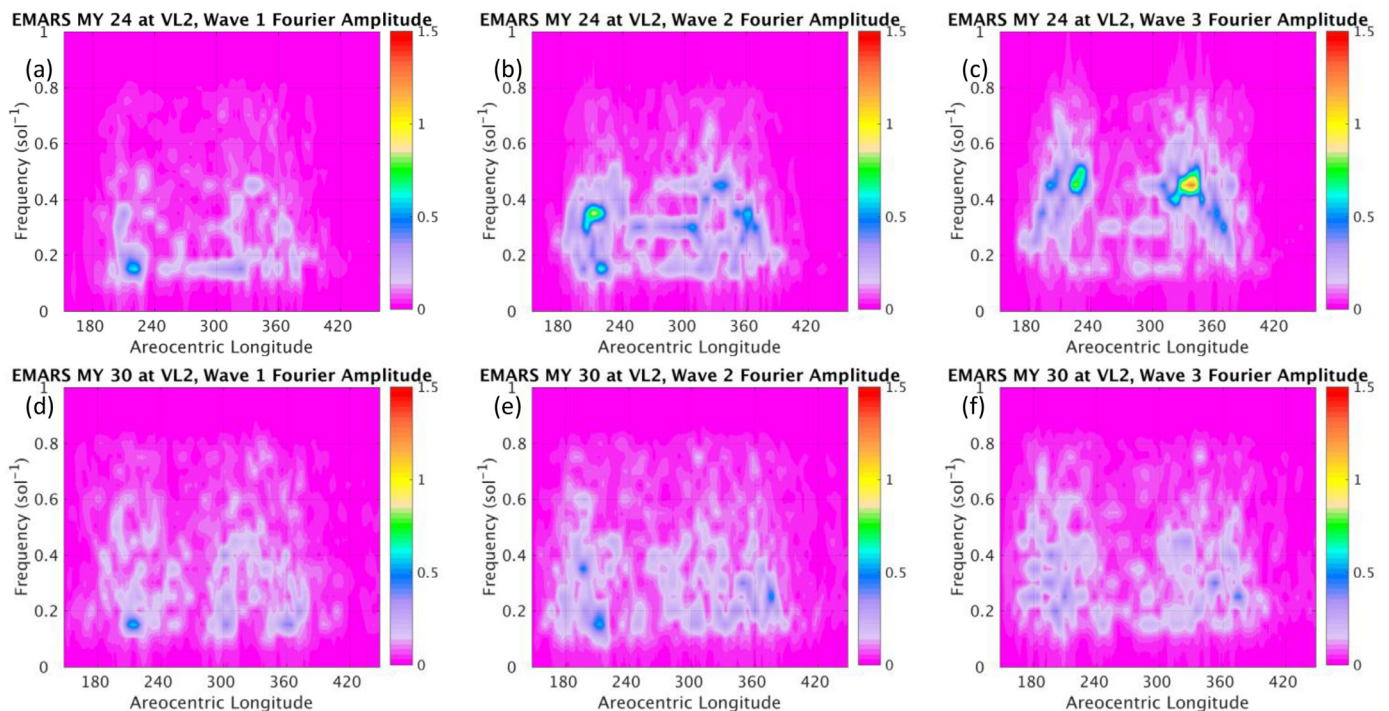


Fig. 20. EMARS Fourier amplitudes of eddy temperature at the model level ~ 1 km above Viking Lander 2 during (a,b,c) MY 24 (TES era) and (d,e,f) MY 30 (MCS era) for zonal wavenumbers (a,d) 1, (b,e) 2, and (c,f) 3.

Table 3

Comparison of the start and end Ls values of waves with wavenumber 3 in MY 24–26 in Hinson et al. (2012) and the corresponding wavenumber 3 periods in EMARS.

MY	Ls (Hinson et al., 2012)		Ls (EMARS)	
	Start	End	Start	End
24	219	230	215	230
	316	339	306	339
25	none	none	none	none
	316	330	308	336
26	228	242	236	240
	306	318	309	317

sols, in agreement with previous studies. Similarly, in MY 24, zonal wave 2 corresponds with a frequency between 0.3 and 0.35 sol⁻¹, or a period between 2.9 and 3.3 sol⁻¹, and zonal wave 3 corresponds with 0.45 sol⁻¹, or 2.2 sols. The MY 24 results provide evidence that the wave periods 6.7, 3.1, and 2.3 sols observed in Viking correspond to observations of zonal waves 1 through 3, and is consistent with results obtained in free running MGCM simulations. Among all the TES years, 7 periods of large zonal wavenumber 3 Fourier amplitude and 2–2.5 sol periods in the pre- and post-solstice seasons correlate with the initiation and presence of dust storms, with the exception of a period of intense wave 3 activity between Ls 340 and 355 in MY 26 (not shown). In MY 30, zonal wave 1 has a dominant 6.7 sol period, the same as in MY 24. However, no single period is dominant for zonal waves 2 and 3 in MY 30. The zonal wavenumber / wave period relationship for MCS EMARS is therefore less clear than for TES EMARS, and further evidence that the MCS EMARS has greater difficulty in locking into a cleanly propagating wave.

An additional independent source of information on Mars atmosphere transient eddies comes from the Mars Global Surveyor radio science data. Hinson (2006), Table 2 provides a listing of northern hemisphere wave regimes inferred from radio science. The zonal wave 3 found in radio science in MY 25 Ls 315–334 is present in both EMARS and MACDA (more consistently in EMARS), as well as the zonal wave 3 at MY 26 Ls 226–238 (more consistently in MACDA). Zonal wave 2 (MY 26 Ls 20–27 and 190–200) is also found in radio science and both reanalyses. A dominant wavenumber 1 is comparatively rare in EMARS/MACDA during the TES era compared to radio science. Table 3 compares the start and end times, in Ls, of periods of significant zonal wave 3 activity in Table 1 of Hinson et al. (2012) with corresponding periods of dominance of wave 3 in EMARS (Fig. 15). For each period where Hinson et al. (2012) indicate significant zonal wavenumber 3 activity and EMARS reanalysis data is available, there is some overlap with exactly one period when wavenumber 3 is dominant in EMARS, and the start and end times of those periods are given in Table 3. In five seasons out of six, there is agreement in the end times of the wavenumber activity between EMARS and Hinson et al. (2012), with differences of 2 Ls or less. Both EMARS and Hinson et al. (2012) agree that there is no significant wave 3 activity in the fall of MY 25. There is less agreement in the start time of wavenumber 3 activity, and there are times in EMARS when wavenumber 3 dominates that are not mentioned in Table 1 of Hinson et al. (2012). One caveat is that radio science samples only a single latitude, whereas the wave regimes characterized in Fig. 15 use the latitude of greatest eddy amplitude.

3.6. Synoptic maps of weather systems

An important goal of reanalyses is to characterize the complete synoptic state of the atmosphere, describing the temperature, wind, pressure, and aerosol fields as closely as possible to the “true” Mars atmosphere state. This capability enables case studies of significant weather events, including the initiation and development of regional dust storms. Fig. 1a gave such an example of a synoptic map for EMARS

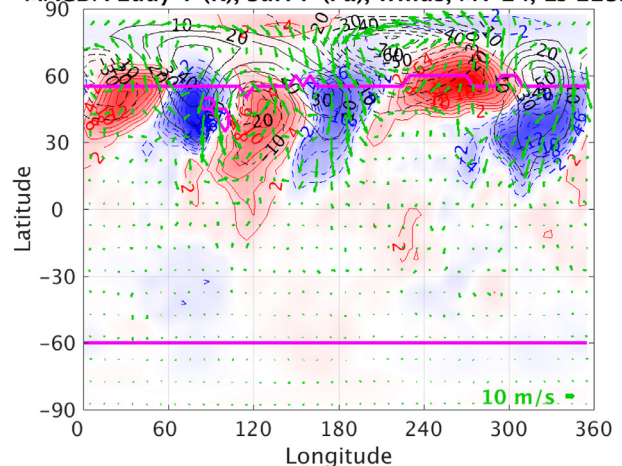
MACDA Eddy T (K), Surf P (Pa), Winds, MY 24, Ls 223.87

Fig. 21. Synoptic map at the same time as Fig. 1, except for MACDA plotted at model level 8 (sigma 0.9).

around the time a cross-equatorial storm was occurring. For comparison, Fig. 21 shows a synoptic map of MACDA at the same time. (It should be noted that the Ls values in MACDA were intended to serve as a seasonal index and be accurate to the nearest sol; the sol number and hour in MACDA should be used to correctly match to the appropriate time in EMARS; L. Montabone, personal communication). Note the synoptic scale similarities between the reanalyses: a zonal wave 3 eddy spans the northern hemisphere, with local areas of low pressure found near longitudes 15, 120, and 220 E. While the large scales are in general agreement, smaller scale details will vary; these are a function of the underlying model and assimilation system used in the reanalyses. There are strong winds blowing north to south at longitude 170 E; these winds are lifting dust and transporting it southward. MOC imagery can provide additional validation of reanalyses (e.g. Mooring and Wilson, 2015) by identifying dust fronts and other visible features, and relating them to the eddy structure in reanalyses.

4. Conclusions

Transient eddies in the lower atmosphere (generally below 300 Pa) in multiple reanalyses are explored comprehensively for the first time. This includes a comparison of waves derived from 3 years of TES and 3 years of MCS observations, in both MACDA and EMARS, as well as with independent observations. Eddy activity tends to last from around Ls 160 to Ls 60 in the NH, and Ls 0 to Ls 200–240 in the SH each year, with peak temperature amplitudes around 10 K. While zonal wavenumbers 1 to 3 are always present, a dominant wave regime can be assigned based on the wavenumber with the largest amplitude. These wave regimes exhibit chaotic fluctuations and interannual variability, although there are some seasons with preferred regimes (wave 2 in autumn; wave 3 in spring). Notably, these are the pre- and post-solstice seasons when cross-equatorial regional (or so-called flushing storms) are particularly prominent in most years; these are the “A” and “C” storm periods described by Kass et al. (2016).

There are some systematic differences in eddies between EMARS using TES observations and EMARS using MCS observations that are likely beyond natural interannual variability. These may be due to systematic differences in the instruments and retrievals and how they are processed via data assimilation. Spurious differences between MY 26 and MY 24/25 likely arise from TES instrument errors. The MCS eddies in the ensemble mean have somewhat smaller amplitudes and extend further into spring in the SH (Ls 240 vs Ls 200). Another systematic difference is that MCS has stronger SH eddies and weaker NH eddies compared to TES. Several recent studies show that the SH eddy

season and amplitude is sensitive to dust and ice cloud forcing in model simulations. In Mulholland et al. (2016) Fig. 3, changing the dust distribution and presence / absence of radiatively active water ice clouds in the UK GCM can significantly modify the amplitude and seasonality of southern hemisphere eddies. Similar sensitivities are found in Lee et al. (2018) Fig. 7 with the MarsWRF GCM. Therefore, there is modeling evidence that the SH wave season can extend well beyond Ls 200. Although both TES and MCS EMARS have somewhat similar dust and ice cloud model settings, the MCS has greater vertical resolution and may have different implied aerosol heating and vertical temperature structure and therefore wave climatologies in its respective reanalysis. TES and MCS also have different dust amounts near the CO₂ ice cap edge (e.g. Montabone et al., 2015). The reduced observation coverage for MCS near the surface may be one of the reasons for the differences in eddy behavior.

Whereas the TES ensemble mean and individual member eddy amplitudes are similar, the MCS ensemble mean is weaker than individual members. This indicates a lack of complete convergence of the ensemble, and indicates the observations may be insufficient to constrain the phase of the transient eddies. MCS misses data in the lowest few km of the atmosphere, due to its limb geometry and sensitivity to aerosol loading. Therefore, reanalyses (especially for MCS) are incomplete without some measure of confidence in the convergence of the transient eddy state; this can be provided by an ensemble, as shown in a figure with each individual member plotted. These systematic differences between TES and MCS waves is an area of further investigation.

Wave properties in MACDA and EMARS generally agree much more closely with one another than with their underlying control run (model simulations without data assimilation). As EMARS is an ensemble reanalysis, the ensemble mean provides the best estimate of the phase of the transient eddies, the ensemble spread characterizes its uncertainty, and individual members provide a representative eddy amplitude and structure. Wave phases within the EMARS ensemble generally converge (especially for TES), and there are generally good agreement on wave phase between EMARS and MACDA. Experiments that vary aspects of the assimilation system and model also demonstrate a robustness of the waves in EMARS. The reanalyses also generally agree with eddy surface pressure amplitudes from Viking in-situ observations, and wave regimes characterized from MGS radio science measurements. A wave with a ~2.3 sol period in the Viking data is also found in the reanalyses sampled at Viking lander locations; this wave is linked to regional dust storms and a zonal wavenumber 3 pattern. The value of the Viking surface pressure data, given the lack of other direct constraints on surface pressure, is demonstrated here. Future observing systems that include surface pressure measurements would be very useful in constraining transient eddies in reanalyses, as well as resolving differences in eddy characteristics between TES and MCS reanalyses. Surface pressure observations in the mid-latitudes are of particular value because they help constrain both the mass and wind field (using geostrophic balance), and wind observations on Mars are currently lacking. Given the wavenumber / wave period relationship on Mars, even a single mid-latitude pressure measurement could provide wavenumber regime and phase information for validating reanalyses. A network of surface pressure stations would be of particular value in constraining eddy structure. Synoptic maps also show agreement of large scale features, whereas the details may be dependent upon the information content of the observations, and the configuration of the underlying model and assimilation scheme. As models and assimilation systems become more sophisticated (for example, in the assimilation of aerosols; e.g. Navarro et al., 2014; 2017), we expect the fidelity of reanalyses to also improve. Reanalyses serve as a useful tool for examining the climatology and interannual variability of Martian weather, as well as for

case studies of particular dust storms.

Acknowledgments

We are most grateful for the scientific contributions toward the development of EMARS by Eugenia Kalnay, Ross Hoffman, Thomas Nehr Korn, Mark Leidner, Yongjing Zhao, Matthew Wespetal and others. We thank the MCS team, including Dan McCleese, David Kass, and Armin Kleinböhl, for insights on using the MCS observations for data assimilation; and Luca Montabone for active discussions on comparing EMARS and MACDA. The UK MACDA control simulation, created by Luca Montabone, Stephen Lewis, Peter Read, and collaborators, was provided directly to the authors by Luca Montabone. To request access to the control simulation, contact the MACDA team at lmontabone@SpaceScience.org. We thank two reviewers, Michael Battalio and Jeff Barnes, for very insightful feedback that helped improve this paper. This research made use of computational resources provided by the Penn State Department of CyberScience. This research was funded by NASA MDPAP grants NNX11AL25G, NNX14AM13G and 80NSSC17K0690.

Supplementary materials

Supplementary material associated with this article can be found, in the online version, at doi:10.1016/j.icarus.2018.07.001.

References

- Banfield, D., Conrath, B.J., Gierasch, P.J., Wilson, R.J., Smith, M.D., 2004. Traveling waves in the Martian atmosphere from MGS TES Nadir data. *Icarus* 170, 365–403. <https://doi.org/10.1016/j.icarus.2004.03.015>.
- Barnes, J.R., 1980. Time spectral analysis of midlatitude disturbances in the Martian atmosphere. *J. Atmos. Sci.* 37, 2002–2015.
- Barnes, J.R., Pollack, J.B., Haberle, R.M., Leovy, C.B., Zurek, R.W., Lee, H., Schaeffer, J., 1993. Mars atmospheric dynamics as simulated by the NASA Ames General Circulation Model: 2. Transient baroclinic eddies. *J. Geophys. Res. Planets* 98 (E2), 3125–3148.
- Barnes, J.R., 2006. FFSM studies of transient eddies in the MGCM TES temperature data. In: *Proceedings of the Second Workshop on Mars Atmosphere Modelling and Observations*. Granada, Spain. Feb 27-Mar 3, 2006.
- Book chapter Barnes, J.R., Haberle, R.M., Wilson, R.J., Lewis, S.R., Murphy, J.R., Read, P.L., 2017. The global circulation. In: Haberle, R.M., Clancy, R.T., Forget, F., Smith, M.D., Zurek, R.W. (Eds.), *The Atmosphere and Climate of Mars*. Cambridge University Press, Cambridge, UK.
- Basu, S., Wilson, J., Richardson, M., Ingersoll, A., 2006. Simulation of spontaneous and variable global dust storms with the GFDL Mars GCM. *J. Geophys. Res. Planets* 111 (E9). <https://doi.org/10.1029/2005JE002660>.
- Battalio, M., Szunyogh, I., Lemmon, M., 2016. Energetics of the Martian atmosphere using the Mars Analysis Correction Data Assimilation (MACDA) dataset. *Icarus* 276, 1–20. <https://doi.org/10.1016/j.icarus.2016.04.028>.
- Battalio, M., Szunyogh, I., Lemmon, M., 2018. Wave energetics of the southern hemisphere of Mars. *Icarus* 309, 220–240. <https://doi.org/10.1016/j.icarus.2018.03.015>.
- Cantor, B.A., James, P.B., Caplinger, M., Wolff, M.J., 2001. Martian dust storms: 1999 Mars Orbiter camera observations. *J. Geophys. Res. Planets* 106 (E10), 23653–23687.
- Cantor, B.A., 2007. MOC observations of the 2001 Mars planet-encircling dust storm. *Icarus* 186, 60–96. <https://doi.org/10.1016/j.icarus.2006.08.019>.
- Clancy, R.T., Sandor, B.J., Wolff, M.J., Christensen, P.R., Smith, M.D., Pearl, J.C., Conrath, B.J., Wilson, R.J., 2000. An intercomparison of ground-based millimeter, MGS TES, and Viking atmospheric temperature measurements: seasonal and inter-annual variability of temperatures and dust loading in the global Mars atmosphere. *J. Geophys. Res.* 105 (E4), 9553–9571.
- Colaprete, A., Barnes, J.R., Haberle, R.M., Montmessin, F., 2008. CO₂ clouds, CAPE and convection on Mars: observations and general circulation modeling. *Planet. Space Sci.* 56 (2), 150–180. <https://doi.org/10.1016/j.pss.2007.08.010>.
- Collins, M., Lewis, S.R., Read, P.L., Hourdin, F., 1996. Baroclinic wave transitions in the Martian atmosphere. *Icarus* 120, 344–357.
- Conrath, B.J., 1975. Thermal structure of the Martian atmosphere during the dissipation of the dust storm of 1971. *Icarus* 24, 36–46.
- Desroziers, G., Berre, L., Chapnik, B., Poli, P., 2005. Diagnosis of observation, background, and analysis-error statistics in observation space. *Q. J. R. Meteorol. Soc.* 131, 3385–3396. <https://doi.org/10.1256/qj.05.108>.
- Eluszkiewicz, J., Moncet, J.-L., Shephard, M.W., Cady-Pereira, K., Connor, T., Uymin, G., 2008. Atmospheric and surface retrievals in the Mars polar regions from the Thermal

- Emission Spectrometer measurements. *J. Geophys. Res.* 113, E10010. <https://doi.org/10.1029/2008JE003120>.
- Evensen, G., 1994. Sequential data assimilation with a nonlinear quasi-geostrophic model using Monte Carlo methods to forecast error statistics. *J. Geophys. Res.* 99 (C5), 10143–10162.
- Forget, F., Hourdin, F., Fournier, R., Hourdin, C., Talagrand, O., Collins, M., Lewis, S.R., Read, P.L., Huot, J.-P., 1999. Improved general circulation models of the Martian atmosphere from the surface to above 80km. *J. Geophys. Res.* 104 (E10), 24155–24175.
- Greybush, S.J., Kalnay, E., Miyoshi, T., Ide, K., Hunt, B.R., 2011. Balance and ensemble Kalman filter localization techniques. *Mon. Wea. Rev.* 139, 511–522. <https://doi.org/10.1175/2010MWR3328.1>.
- Greybush, S.J., Kalnay, E., Ide, K., Miyoshi, T., McConnochie, T., Hoffman, M.J., Hoffman, R.N., Wilson, R.J., 2012. Ensemble Kalman Filter Data Assimilation of Thermal Emission Spectrometer (TES) Profiles into a Mars global circulation model. *J. Geophys. Res. Planets* 117, E11008. <https://doi.org/10.1029/2012JE004097>.
- Greybush, S.J., Kalnay, E., Hoffman, M.J., Wilson, R.J., 2013. Identifying Martian atmospheric instabilities and their physical origins using Bred vectors. *Q. J. R. Meteorol. Soc.* 139, 639–653. <https://doi.org/10.1002/qj.1990>.
- Haberle, R.M., Juarez, M.T., Kahre, M.A., Kass, D.M., Barnes, J.R., Hollingsworth, J.L., Harri, A.-M., Kahanpaa, H., 2018. Detection of Northern Hemisphere transient eddies at Gale Crater. *Icarus* 307, 150–160.
- Hinson, D.P., 2006. Radio occultation measurements of transient eddies in the northern hemisphere of Mars. *J. Geophys. Res.* 111, E05002. <https://doi.org/10.1029/2005JE002612>.
- Hinson, D.P., Wang, H.Q., 2010. Further observations of regional dust storms and baroclinic eddies in the northern hemisphere of Mars. *Icarus* 206, 290–305.
- Hinson, D.P., Wang, H., Smith, M.D., 2012. A multi-year survey of dynamics near the surface in the northern hemisphere of Mars: short-period baroclinic waves and dust storms. *Icarus* 219, 307–320. <https://doi.org/10.1016/j.icarus.2012.03.001>.
- Hoffman, M.J., Greybush, S.J., Wilson, R.J., Gyarmati, G., Hoffman, R.N., Kalnay, E., Ide, K., Kostelich, E.J., Miyoshi, T., Szunyogh, I., 2010. An ensemble Kalman filter data assimilation system for the Martian atmosphere: implementation and simulation experiments. *Icarus* 209, 470–481. <https://doi.org/10.1016/j.icarus.2010.03.034>.
- Hoffman, R.N., 2010. A retrieval strategy for interactive ensemble data assimilation. <http://arxiv.org/abs/1009.1561>.
- Hoffman, M.J., Eluszkiewicz, J., Weisenstein, D., Uymin, G., Moncet, J.-L., 2012. Assessment of Mars atmospheric temperature retrievals from the thermal emission spectrometer radiances. *Icarus* 220 (2), 1031–1039. <https://doi.org/10.1016/j.icarus.2012.06.039>. 2012.
- Hollingsworth, J.L., Kahre, M.A., 2010. Extratropical cyclones, frontal waves, and Mars dust: modeling and considerations. *Geophys. Res. Lett.* 37, L22202. <https://doi.org/10.1029/2010GL044262>.
- Hollingsworth, J.L., Haberle, R.M., Barnes, J.R., Bridger, A.F.C., Pollack, J.B., Lee, H., Schaeffer, J., 1996. Orographic control of storm zones on Mars. *Nature* 380, 413–416.
- Houben, H., 1999. Assimilation of Mars Global Surveyor meteorological data. *Adv. Space Res.* 23 (11), 1899–1902.
- Hunt, B.R., Kostelich, E.J., Szunyogh, I., 2007. Efficient data assimilation for spatio-temporal chaos: a local ensemble transform Kalman filter. *Physica D* 230, 112–126. <https://doi.org/10.1016/j.physd.2006.11.008>.
- Kahre, M.A., Wilson, R.J., Haberle, R.M., Hollingsworth, J.L., 2009. An inverse approach to modeling the dust cycle with two Mars general circulation models. In: *Proceedings of the Mars Dust Cycle Workshop, NASA/Ames Research Center, CA*.
- Kalnay, E., Kanamitsu, M., Kistler, R., Collins, W., Deaven, D., Gandin, L., Iredell, M., Saha, S., White, G., Woollen, J., Zhu, Y., Leetmaa, A., Reynolds, R., Chelliah, M., Ebisuzaki, W., Higgins, W., Janowiak, J., Mo, K.C., Ropelewski, C., Wang, J., Jenne, R., Joseph, D., 1996. The NCEP/NCAR 40-year reanalysis project. *Bull. Amer. Meteor. Soc.* 77, 437–471.
- Kalnay, E., Li, H., Miyoshi, T., Yang, S.-C., Ballabrera-Poy, J., 2007. 4-D-Var or ensemble Kalman Filter? *Tellus* 59 (5), 758–773. <https://doi.org/10.1111/j.1600-0870.2007.00261.x>.
- Kass, D.M., Kleinböhl, A., McCleese, D.J., Schofield, J.T., Smith, M.D., 2016. Interannual similarity in the Martian atmosphere during the dust storm season. *Geophys. Res. Lett.* 43, 6111–6118. <https://doi.org/10.1002/2016GL068978>.
- Kavulich, M.J., Szunyogh, I., Gyarmati, G., Wilson, R.J., 2013. Local dynamics of baroclinic waves in the Martian atmosphere. *J. Atmos. Sci.* 70, 3415–3446. <https://doi.org/10.1175/JAS-D-12-0262.1>.
- Kleinböhl, A., Schofield, J.T., Kass, D.M., Abdou, W.A., Backus, C.R., Sen, B., Shirley, J.H., Lawson, W.G., Richardson, M.I., Taylor, F.W., Teanby, N.A., McCleese, D.J., 2009. Mars Climate Sounder limb profile retrieval of atmospheric temperature, pressure, and dust and water ice opacity. *J. Geophys. Res.* 114, E10006. <https://doi.org/10.1029/2009JE003358>.
- Kleinböhl, A., Wilson, R.J., Kass, D., Schofield, J.T., McCleese, D.J., 2013. The semi-diurnal tide in the middle atmosphere of Mars. *Geophys. Res. Lett.* 40. <https://doi.org/10.1002/grl.50497>.
- Kleinböhl, A., Friedson, A.J., Schofield, J.T., 2017. Two-dimensional radiative transfer for the retrieval of limb emission measurements in the Martian atmosphere. *JQSRT* 187, 511–522.
- Lee, C., Lawson, W.G., Richardson, M.I., Anderson, J.L., Collins, N., Hoar, T., Mischna, M., 2011. Demonstration of ensemble data assimilation for Mars using DART, MarsWRF, and radiance observations from MGS TES. *J. Geophys. Res.* 116, E11011. <https://doi.org/10.1029/2011JE003815>.
- Lee, C., Richardson, M.I., Newman, C.E., Mischna, M.A., 2018. The sensitivity of solstitial pauses to atmospheric ice and dust in the MarsWRF General Circulation Model. *Icarus* 311, 23–34. <https://doi.org/10.1016/j.icarus.2018.03.019>.
- Lewis, S.R., Read, P.L., 1995. An operational data assimilation scheme for the Martian atmosphere. *Adv. Space Res.* 16 (6), 9–13.
- Lewis, S.R., Read, P.L., Conrath, B.J., Pearl, J.C., Smith, M.D., 2007. Assimilation of Thermal Emission Spectrometer atmospheric data during the Mars Global Surveyor aerobraking period. *Icarus* 192 (2), 327–347. <https://doi.org/10.1016/j.icarus.2007.08.009>.
- Lewis, S.R., Mulholland, D.P., Read, P.L., Montabone, L., Wilson, R.J., Smith, M.D., 2016. The solstitial pause on Mars: 1. A planetary wave reanalysis. *Icarus* 264, 456–464. <https://doi.org/10.1016/j.icarus.2015.08.039>.
- Lorenc, A.C., Bell, R.S., Macpherson, B., 1991. The meteorological office analysis correction data assimilation scheme. *Q. J. R. Meteorol. Soc.* 117 (497), 59–89. <https://doi.org/10.1002/qj.49711749704>.
- McCleese, D.J., Schofield, J.T., Taylor, F.W., Calcutt, S.B., Foote, M.C., Kass, D.M., Leovy, C.B., Paige, D.A., Read, P.L., Zurek, R.W., 2007. Mars Climate Sounder: an investigation of thermal and water vapor structure, dust and condensate distributions in the atmosphere, and energy balance of the polar regions. *J. Geophys. Res.* 112, E05S06. <https://doi.org/10.1029/2006JE002790>.
- Miyoshi, T., 2011. The Gaussian approach to adaptive covariance inflation and its implementation with the local ensemble transform Kalman filter. *Mon. Wea. Rev.* 139, 1519–1535. <https://doi.org/10.1175/2010MWR3570.1>.
- Moncet, J.-L., Uymin, G., Lipton, A.E., Snell, H.E., 2008. Infrared radiance modeling by optimal spectral sampling. *J. Atmos. Sci.* 65, 3917–3934. <https://doi.org/10.1175/2008JAS2711.1>.
- Montabone, L., Lewis, S.R., Read, P.L., Hinson, D.P., 2006. Validation of martian meteorological data assimilation for MGS/TES using radio occultation measurements. *Icarus* 185, 113–132. <https://doi.org/10.1016/j.icarus.2006.07.012>.
- Montabone, L., Marsh, K., Lewis, S.R., Read, P.L., Smith, M.D., Holmes, J., Spiga, A., Lowe, D., Pamment, A., 2014. The Mars Analysis Correction Data Assimilation (MACDA) Dataset V1.0. *Geosci. Data J.* 1 (2), 129–139. <https://doi.org/10.1002/gdj3.13>.
- Montabone, L., Forget, F., Millour, E., Wilson, R.J., Lewis, S.R., Cantor, B., Cass, D., Kleinboehl, A., Lemmon, M.T., Smith, M.D., Wolff, M.J., 2015. Eight-year climatology of dust optical depth on Mars. *Icarus* 251, 65–95. <https://doi.org/10.1016/j.icarus.2014.12.034>.
- Montmessin, F., Forget, F., Rannou, P., Cabane, M., Haberle, R.M., 2004. Origin and role of water ice clouds in the Martian water cycle as inferred from a general circulation model. *J. Geophys. Res.* 109, E10004. <https://doi.org/10.1029/2004JE002284>.
- Mooring, T.A., Wilson, R.J., 2015. Transient eddies in the MACDA Mars reanalysis. *J. Geophys. Res. Planets* 120, 1671–1696. <https://doi.org/10.1002/2015JE004824>.
- Mulholland, D.P., Lewis, S.R., Read, P.L., Madeleine, J.-B., Forget, F., 2016. The solstitial pause on Mars: 2 modelling and investigation of causes. *Icarus* 264, 465–477. <https://doi.org/10.1016/j.icarus.2015.08.038>.
- Navarro, T., Forget, F., Millour, E., Greybush, S.J., 2014. Detection of detached dust layers in the Martian atmosphere from their thermal signature using assimilation. *Geophys. Res. Lett.* 41, 6620–6626. <https://doi.org/10.1002/2014GL061377>.
- Navarro, T., Forget, F., Millour, E., Greybush, S.J., Kalnay, E., Miyoshi, T., 2017. The challenge of atmospheric data assimilation on Mars. *Earth Space Sci.* 4 (12), 690–722. <https://doi.org/10.1002/2017EA000274>.
- Pankine, A.A., 2015. The nature of the systematic radiometric error in the MGS TES spectra. *Planet. Space Sci.* 109, 64–75.
- Pankine, A.A., 2016. Radiometric error and re-calibration of the MGS TES spectra. *Planet. Space Sci.* 134, 112–121. <https://doi.org/10.1016/j.pss.2016.10.105>.
- Pottier, A.F., Forget, F., Montmessin, F., Navarro, T., Spiga, A., Millour, E., Szantai, A., Madeleine, J.-B., 2017. Unraveling the martian water cycle with high-resolution global climate simulations. *Icarus* 291, 82–106. <https://doi.org/10.1016/j.icarus.2017.02.016>.
- Shirley, J.H., McConnochie, T.H., Kass, D.M., Kleinboehl, A., Schofield, J.T., Heavens, N.G., McCleese, D.J., Benson, J., Hinson, D.P., Bandfield, J.L., 2015. Temperatures and aerosol opacities of the Mars atmosphere at aphelion: validation and inter-comparison of limb sounding profiles from MRO/MCS and MGS/TES. *Icarus* 251, 26–49. <https://doi.org/10.1016/j.icarus.2014.05.011>.
- Smith, M.D., Pearl, J.C., Conrath, B.J., Christensen, P.R., 2001. Thermal Emission Spectrometer results: Mars atmospheric thermal structure and aerosol distribution. *J. Geophys. Res.* 106 (E10), 23929–23945.
- Steele, L.J., Lewis, S.R., Patel, M.R., Montmessin, F., Forget, F., Smith, M.D., 2014. The seasonal cycle of water vapour on Mars from assimilation of thermal emission spectrometer data. *Icarus* 237, 97–115. <https://doi.org/10.1016/j.icarus.2014.04.017>.
- Strausberg, M.J., Wang, H., Richardson, M.I., Ewald, S.P., Toigo, A.D., 2005. Observations of the initiation and evolution of the 2001 Mars global dust storm. *J. Geophys. Res.* 110, E02006. <https://doi.org/10.1029/2004JE002361>.
- Wang, H., Richardson, M.I., 2015. The origin, evolution, and trajectory of large dust storms on Mars during Mars years 24–30 (1999–2011). *Icarus* 251, 112–127. <https://doi.org/10.1016/j.icarus.2013.10.033>.
- Wang, H., Richardson, M.I., Wilson, R.J., Ingersoll, A.P., Toigo, A.D., Zurek, R.W., 2003. Cyclones, tides, and the origin of a cross-equatorial dust storm on Mars. *Geophys. Res. Lett.* 30, 1488. <https://doi.org/10.1029/2002GL016828>.
- Wang, H., Zurek, R.W., Richardson, M.I., 2005. Relationship between frontal dust storms and transient eddy activity in the northern hemisphere of Mars as observed by Mars Global Surveyor. *J. Geophys. Res.* 110. <https://doi.org/10.1029/2005JE002423>.
- Wang, H., Toigo, A.D., Richardson, M.I., 2011. Curvilinear features in the southern hemisphere observed by Mars global surveyor Mars orbiter camera. *Icarus* 215 (2011), 242–252. <https://doi.org/10.1016/j.icarus.2011.06.029>.
- Wang, H., Richardson, M.I., Toigo, A.D., Newman, C.E., 2013. Zonal wavenumber three traveling waves in the northern hemisphere of Mars simulated with a general circulation model. *Icarus* 223 (2), 654–676. <https://doi.org/10.1016/j.icarus.2013.01.004>.

- Wang, H., Toigo, A.D., 2016. The variability, structure and energy conversion of the northern hemisphere traveling waves simulated in a Mars general circulation model. *Icarus* 271, 207–221. <https://doi.org/10.1016/j.icarus.2016.02.005>.
- Waugh, D.W., Toigo, A.D., Guzewich, S.D., Greybush, S.J., Wilson, R.J., Montabone, L., 2016. Martian polar vortices: comparison of reanalyses. *J. Geophys. Res. Planets* 121, 1770–1785. <https://doi.org/10.1002/2016JE005093>.
- Wilson, R.J., Hamilton, K.P., 1996. Comprehensive model simulation of thermal tides in the Martian atmosphere. *J. Atmos. Sci.* 53 (9), 1290–1326.
- Wilson, R.J., Banfield, D., Conrath, B.J., Smith, M.D., 2002. Traveling waves in the northern hemisphere of Mars. *Geophys. Res. Lett.* 29, 1684–1687. <https://doi.org/10.1029/2002GL014866>.
- Wilson, R.J., Greybush, S.J., Montabone, L., McConnochie, T.H., Kass, D., 2014. Assessment of seasonal and interannual variability in TES and MCS observations. In: *Proceedings of the Eighth International Conference on Mars*. Pasadena, CA. Julyoral presentation.
- Zhang, K.Q., Ingersoll, A.P., Kass, D.M., Pearl, J.C., Smith, M.D., Conrath, B.J., Haberle, R.M., 2001. Assimilation of Mars global surveyor atmospheric temperature data into a general circulation model. *J. Geophys. Res.* 106 (32), 863–877. <https://doi.org/10.1029/2000JE001330>.
- Zhao, Y., Greybush, S.J., Wilson, R.J., Hoffman, R.N., Kalnay, E., 2015. Impact of assimilation window length on diurnal features in a Mars atmospheric analysis. *Tellus A* 67, 26042. <https://doi.org/10.3402/tellusa.v67.26042>.